CNRS
Centre National de la Recherche Scientifique

INFN
Instituto Nazionale di Fisica Nucleare

Advanced Virgo calibration for O2: photodiode sensing and mirror and marionette actuator responses

D. Estevez, V. Germain, F. Marion, B. Mours, L. Rolland, D.Verkindt

VIR-0707C-17

June 4, 2018

VIRGO * A joint CNRS-INFN Project
Project office: Traversa H di via Macerata - I-56021 S. Stefano a Macerata, Cascina (PI)
Secretariat: Telephone (39) 50 752 521 – Fax (39) 50 752 550 – e-mail virgo@pisa.infn.it

Contents

1 Introduction

This note gives the status of the Advanced Virgo calibration during its first participation to the advanced detectors Science Runs, the O2 run. Virgo joined LIGO for the end of O2 run, from 1st August to 25 August 2017. All the mirror and marionette actuators that were used during the run, as well as the sensing of the dark fringe photodiodes (B1), have to be calibrated since they are used in the h(t)-reconstruction process. The purpose of this note is to summarize the overall calibration procedure (measurements and analysis), to study the stability of the calibration parameters and to give the actuation models for the O2 run.

The calibration of the photodiode sensing chain was done with specific measurements a few days before the start of O2. For the actuator calibration, the data included in the analysis are the data taken the week before the run, during weekly calibration during the run and during post-O2 calibration period. In total, it includes the data from 23rd July to 6th September 2017. The outcome of this note are the models for the photodiode sensing and for the mirror and marionette actuators that are being used for the reprocessing of the reconstructed h(t) using the O2 data.

Preliminary actuation models were released before the run and were used for the online h(t) reconstruction. The data that were used were taken in July and particularly the week before the run. These data are not discussed in this note, but the preliminary models are compared to the final ones in the last section.

First, the timing system, the photodiode sensing chain and its calibration are described in sections 2 and 3. In section 4, an overview of the calibration procedure is given. Then, the analysis of the different calibration measurements is given in the sections 5 to 8: (i) calibration of NI, WI and BS mirrors, (ii) calibration of NE and WE mirrors, (iii) calibration of NE and WE marionettes and (iv) calibration of PR mirror. For points (i) to (iii), the figures show the results fo the West cavity mirrors actuators. The figures for the other mirrors are given in appendix.

In the measurements, different delays that are not part of the actuation itself are included and not corrected at each step. They are subtracted to estimate the actuation delay at the end of the procedure as described in section 9.

The final actuation models and their estimated uncertainties are summarized in section 10, and the pre-O2 models are compared to the new ones in section 11.

In parallel, two others notes have been written: a note [1] (VIR-0706B-17) dedicated to the validation of the $h(t)$ reconstructed channel and to the estimation of the associated amplitude and phase uncertainties, and a note [2] (VIR-0708B-17) dedicated to the validation of the AdVirgo timing during O2.

In this new release, we fixed a few typo found in the previous release VIR-0707B-17, in table 5.

1.1 Main changes from version A to version B of this document

- add an estimation of the absolute precision of the IRIG-B signal in section 2, and add this number in the tables for the photodiode and actuation systematic uncertainties.
- fix the figures of NI and WI mirror actuators (figures of version A were the results of a fit with a single pole).
- fill the sections 8 and 9.1.4 about PR mirror calibration.
- add plots for the delay measurement from CAL to Sc actuation channels in section 4.2 and G.

2 Overview of the timing distribution and photodiode sensing

2.1 Overview of the Virgo Timing distribution

The timing distribution is centralized from a main GPS receiver located in the central building of Virgo.. This receiver provides an IRIG-B signal that is distributed to all the digital electronic devices (ADC, DAC channels, real-time PCs, DSP boards, ...) to both enslave their local clock and provide the timestamp.

The distribution is made via Timing Distribution Boxes connected between them by optical fibers. Then short copper cables (few meters) are used to distribute the signal from the TDBoxes to the digital parts.

In order to distribute the IRIG-B signal from the central building to the end building, long fibers of about 3 km are used. The signal arriving in the end building is delayed by ~ 16 µs compared to the signal provided by the GPS receiver. In order to have all the Virgo digital parts in sync, a 3 km fiber has also been used in the front-end distribution of the central building, so that the signal distributed in the central building is also delayed by 16 µs.

The position of the 1 PPS of the IRIG-B signal provided by the GPS receiver may have some offset with respect to absolute GPS time if the receiver is not well calibrated. This offset had been checked when the GPS receivers were installed for Virgo+ in 2009. The IRIG-B signal of the current GPS receiver has been compared to the 1 PPS of the old receiver GPS (see section 3.1 of note [3]). No offset between the two systems was found within the uncertainties of 4.5 µs. For completeness, this number is reported in table 1.

2.2 Overview of the photodiode sensing

The sensing chain of the AdV photodiodes is shown in the figure 1. It is the same for the B1 and B1p photodiodes: B1 photodiodes are the main dark fringe photodiodes looking at the DC signal after the output mode-cleaners (OMCs) in Science Mode, and B1p photodiodes looking at a pickoff of this beam before the OMCs. B1p is used to calibrate the actuator in free swinging Michelson as described in section 5.

The photodiode output is split into three signals in the pre-amplifier: the *DC* signal from DC to 10 kHz, the less noisy *Audio* signal from 5 Hz to 100 kHz and the *RF* signal from 1 MHz to ~ 100 MHz.

At the end of the chain, the *DC* and *Audio* channels are blended together into a new *Blended* channel, using the *Audio* channel as main channel (i.e. the phase of the *Blended* channel is the same as the phase of the *Audio* channel above a few 10's of hertz). In Science Mode, the main dark fringe signal is the *Blended* channel of B1 photodiode. For the actuator

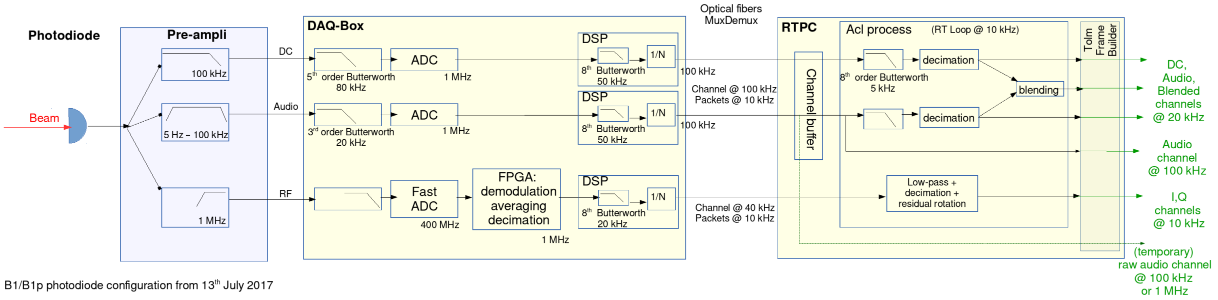

Figure 1: Sketch of the photodiode readout chain. It is the same for both B1 photodiodes and both B1p photodiodes.

calibration in free Michelson, the *DC* channel of the B1p photodiode is used (instead of the *Blended* channel since the *Audio* channel saturates during the measurements).

The ADC channels that aquire the *DC* and *Audio* channels are made of

- a 5th order Butterworth analog filter with a cut-off at 80 kHz
- the ADC chip itself, that samples the input signal at 1 MHz (it is possible to send the raw 1 MHz sampled data to the DAQ directly)
- a DSP that processes low-pass filtering (8th order Butterwoth) and decimation down to 100 kHz
- the output channels are sent to a real-time PC where they are further processed by the Acl software whose is running at 10 kHz:
  - the 100 kHz Audio channel is read and sent to the DAQ without any processing
  - in parallel, both channels are also low-pass filtered and decimated down to 20 kHz, and sent to the DAQ.

The sensing chain response is flat in modulus in the 10 Hz-10 kHz range, but the different steps add delays to be estimated.

3 Calibration of B1p and B1 photodiode readout

The delay of the photodiode sensing chain, from the power on the photodiode to the *Audio* channel stored in the DAQ, has been measured on 26 July 2017, a few days before the start of the run.

The IRIG-B signal from the main GPS receiver of Virgo has been sent to a LED put in front of the B1 and B1p photodiodes. Hence the IRIG-B signal is seen in the stored channels.

The position of the 1 PPS of the IRIG-B in the Virgo frames allows to estimate the delay of the sensing chain. During the measurements, the raw 1 MHz ADC data have been enabled and stored in the data along with the 100 kHz and 20 kHz channels.

3.1 Calibration of the B1p PD1 DC channel

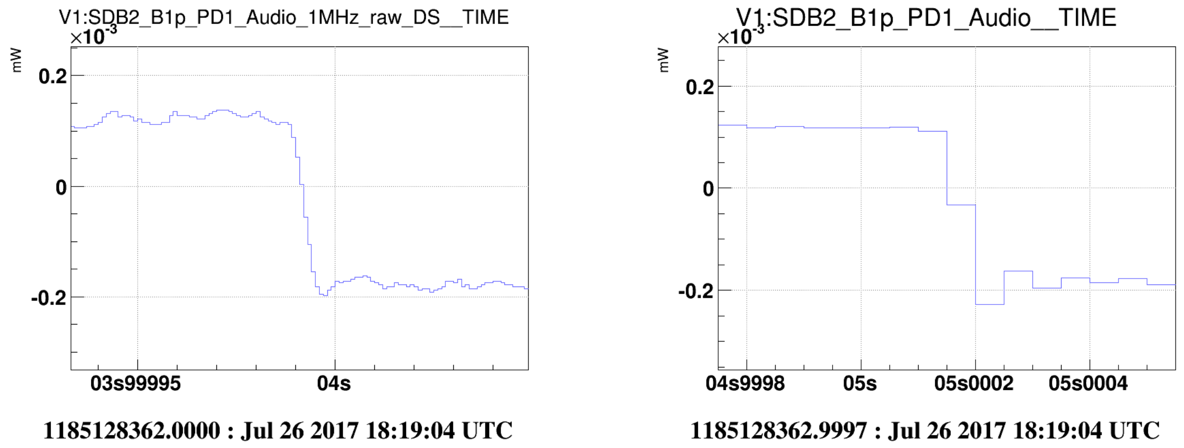

(a) Audio at 1 MHz (b) Audio at 20 kHz

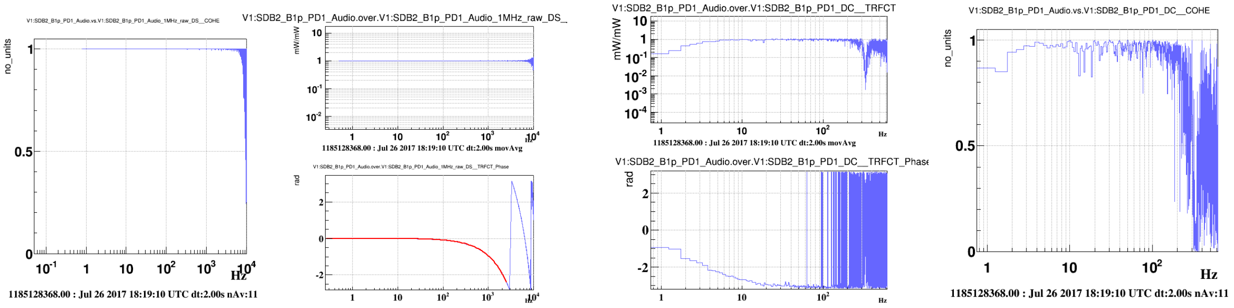

(c) Audio 20 kHz/Audio 1 MHz (d) Audio 20 kHz/DC 20 kHz

Figure 2: Timing calibration of B1p PD1 photodiode.

The *Audio* data sampled at 1 MHz are shown in the figure 2(a), where it is zoomed around the 1 PPS edge inside the IRIG-B signal. The position 1 PPS in the *Audio* channel is about 12 ± 1 µs before the start of the second in the Virgo frames. It corresponds to the expected value:

- ~ 5 µs delay from the analog anti-alias filter,

- ∼ 16 µs advance of all the Virgo data due to the delay in the distribution of the IRIG-B signal to the Virgo digital electronics.

The 1 MHz *Audio* raw data are then processed digitally to compute the *Audio* data sampled at 20 kHz. The *Audio* data sampled at 20 kHz are shown in figure 2(b), also zoomed around the 1 PPS position. From this data, the delay of the 20 kHz channel can be estimated to between 150 and 200 µs, with a precision of one sample of 50 µs.

In order to measure this delay accurately, the transfer function from the 1 MHz to the 20 kHz channel has been computed. It is shown on the figure 2(c). As expected the coherence between the two channels is very good, the modulus is 1 and the phase is consistent with a delay that has been fit to 152 ± 3 µs.

In the free swinging Michelson data, the channel that is used as input for the actuator calibration is the *DC* channel, not the *Audio* channel. In order to check that the *DC* channel has the same delay than the *Audio* channel, the transfer function between both channels has been computed and is shown in figure 2(d). There is a good coherence only up to about 200 Hz since the *DC* channel is noisier. At low frequency, the effect of the high-pass filter in the *Audio* channel path is also visible. But above a few 10's of hertz, the phase converge towards $-\pi$ which is consistent with the *DC* channel having the same delay than the *Audio* channel, but a sign flip.

To conclude, we found that the B1p readout delay of channels *DC* and *Audio* is:

- -12 ± 1 µs from the analog anti-alias filter at the ADC channel input and the Virgo timing distribution system,
- $+152 \pm 3$ µs from the digital processing

Hence, correcting the B1p channel for a delay of 140 µs gives the power arriving on the photodiode at the absolute GPS time, and the systematic uncertainty on this delay is 4 µs.

This value is used for the analysis of the data for the actuator calibration described in this note.

3.2 Calibration of the B1 PD1 and PD2 Blended channels

The B1 PD2 *Audio* data sampled at 1 MHz are shown in the figure **??**, where it is zoomed around the 1 PPS edge inside the IRIG-B signal. As for the B1p photodiode, the position 1 PPS in the *Audio* channel is about 12 ± 1 µs before the start of the second in the Virgo frames and it corresponds to the expected value.

The 1 MHz *Audio* raw data are then processed digitally to compute the *Audio* data sampled at 20 kHz, and the same processing is done on the 1 MHz *DC* raw data. The 20 kHz *Audio*

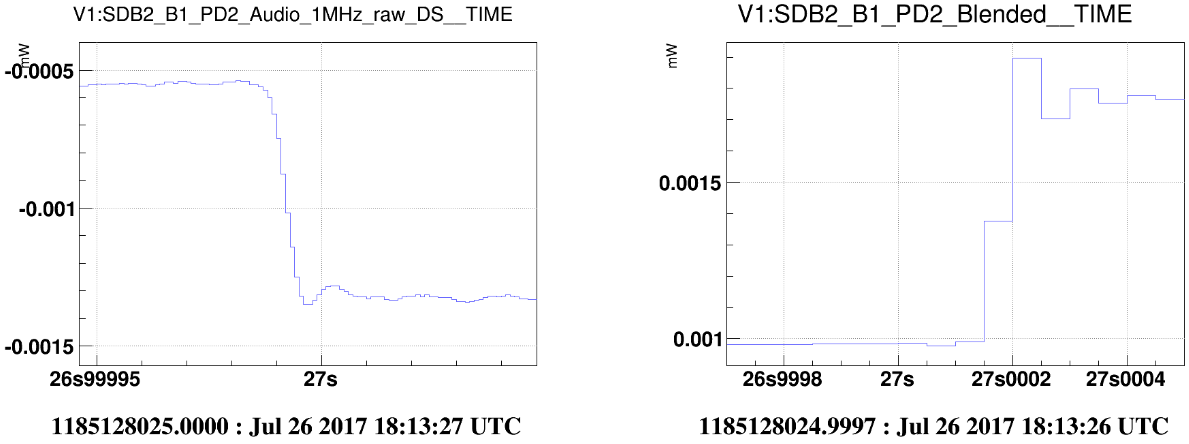

(a) PD2 Audio at 1 MHz (b) PD2 Blended at 20 kHz

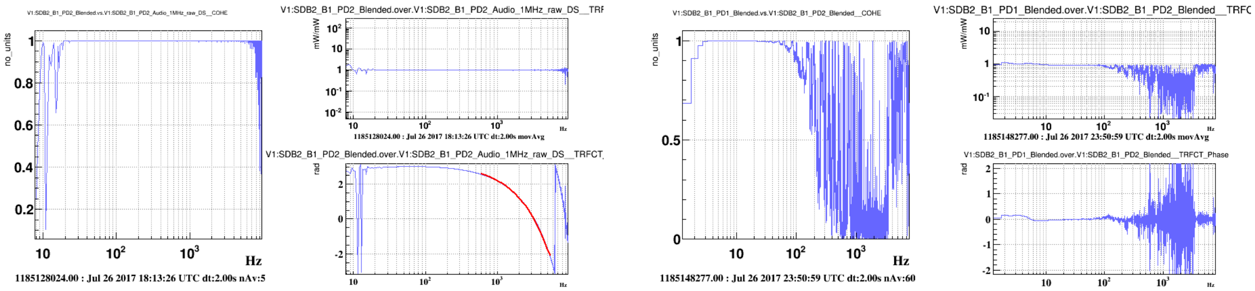

(c) PD2 Blended 20 kHz/Audio 1 MHz (d) Blended PD1/PD2

Figure 3: Timing calibration of B1 PD1 and PD2 photodiodes.

and *DC* channels are finally blended. The *Blended* channel is the one used for the dark fringe signal in the $h(t)$ reconstruction.

The interesting channel for B1 being the *Blended* channel, the time series of this channel is shown on figure 3(b), zoomed around the position of the 1 PPS in the sampled IRIG-B data. As for B1p, the delay is found to be between 150 and 200 µs, within the precision of a sample width of 50 µs.

In order to improve the B1 PD2 delay measurement, the transfer function from the *Audio* channel sampled at 1 MHz to the final *Blended* channel has been computed and is shown figure 3(c). The coherence is good starting from 10 Hz as expected since the lower frequency part of the *Blended* signal comes from the *DC* signal. The phase is consistent with a delay fit to 152 ± 15 µs. The fit uncertainty is larger than for the phase from the 1 MHz to 20 kHz *Audio* channels (which gives, as for B1p, 152 ± 3 µs). This is probably due to some effect of the blending on the phase.

In total, the delay for the B1 PD2 *Blended* channel readout is:

- -12 ± 1 µs from the analog anti-alias filter at the ADC channel input and the Virgo timing distribution system,
- $+152 \pm 15$ µs from the digital processing

In the $h(t)$ reconstruction, the *Blended* channels of both B1 PD1 and PD2 photodiodes are used. Hence the timing of PD1 photodiode must also be estimated. The figure 3(d) gives the transfer function from PD1 to PD2 *Blended* channels during a lock segment on the same date as for the previous PD2 delay measurements. In the range where the coherence between the two photodiodes is good, the phase is around 0 as expected, and there no significant delay between the two photodiodes. Hence the same delay can be used for both B1 photodiodes in the $h(t)$ reconsctrution.

3.3 Summary

The delays for the B1 and B1p photodiode sensing chain are reported in the table 1.

Photodiode channel	*B1p_PD1_DC*	*B1_PD1_Blended*	*B1_PD2_Blended*
Measured delay (µs)	140 ± 4 µs	140 ± 16 µs	140 ± 16 µs
GPS uncertainty (µs)	< 4.5 µs		

Table 1: Summary of the delay from power arriving on the photodiode at a given GPS time to the different photodiode channels stored in the Virgo frames. The upper limit on the offset of the time given by the GPS receiver with respect to the GPS time is also given. Any such offset would be the same for all the Virgo acquired channels.

4 Overview of the actuator calibration procedure

4.1 Overview of an electromagnetic actuator

The Advanced Virgo mirrors and marionettes are driven with electro-magnetic actuators. Four magnets are glued at the back of the mirrors (or similarly on the marionettes). Four coils attached to the mirror reference mass are placed in front of the magnets. Controlling the current flowing inside the coil allows to control the force applied to the mirror and hence its motion. In Advanced Virgo, a single reference mass suspended to the filter F7 of the superattenuator is used for both the marionette and the mirror.

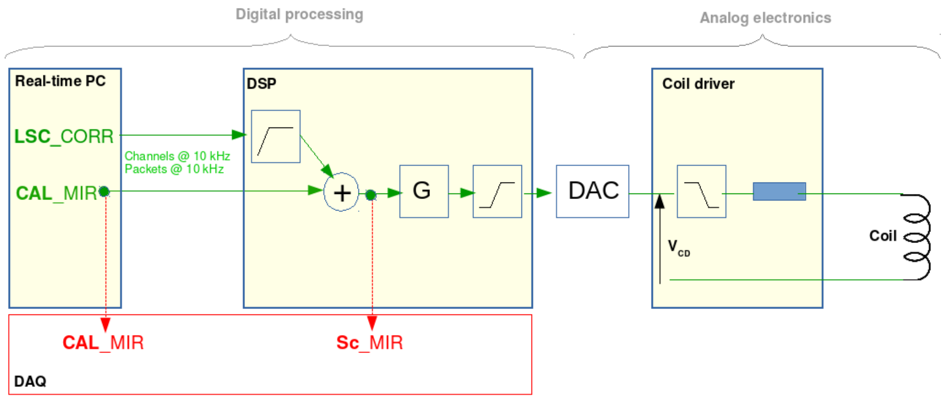

Figure 4: Sketch of the mirror actuation principle. The sketch for the marionette actuation is similar, with channels called MAR instead of MIR, except that the control reallocation is a low-pass filter instead of a high-pass filter. See text for details.

An overview of the actuator principle and the channels that are used in the calibration analysis are shown in the figure 4:

- the channels CAL_MIR (or CAL_MAR) are generated at 10 kHz on a real-time PC whose cycles run at 10 kHz. They are sent to the actuator DSP into packets at 10 kHz.
- in the DSP, the channels are added to the correction signal (after mirror/marionette hierarchical reallocation of the controls). The Sc_MIR signals sent to the DAQ are picked-up at this level[1]. In the DSP, the signal can be processed with a gain and a

---

[1] In the data, the channels are called $CAL\_NE\_MIR\_Z\_CORR$, $CAL\_NE\_MAR\_Z\_CORR$, $Sc\_NE\_MIR\_Z\_CORR$ and $Sc\_NE\_MAR\_Z\_CORR$ (example of NE mirror and marionette channels).. Since the calibration deals only with the longitudinal dof, we removed the Z_CORR part of the names in this note.

shaping filter (first order filter with a zero around 5 Hz and a pole 105 Hz around) and sent to drive a DAC.

- the DAC output drive the voltage V_{CD} at the input of the coil driver. The coil driver is made of a series of resistors, a cable going from the electronics to the coils and back (going along the suspension inside the tower vacuum tank). The coil has some internal resistance and inductance. Hence the coil driver itself is mainly a simple R-L circuit. In addition, a un-shaping filter can be used at the DAC output. The shaping/un-shaping filter combination is used to reduce the DAC noise. They parameters of the digital shaping filter are set to compensate the analog un-shaping filter.

Different types of actuators have been used for the different mirrors during O2:

- NI and WI mirror actuators are in the so-called HighPower (HP) mode: there is no gain nor shaping filter in the DSP, and the total resistor is low ($\sim 30\ \Omega$). Having a large dynamic, these actuators are used for the lock acquisition. But the DAC coil drivers are opened in Science Mode since the DAC noise, applied on the Fabry-Perot cavity length, is limiting the sensitivity curve up to $\sim 200\,\mathrm{Hz}$.
- PR mirror actuator is also in the HighPower mode, and is used to control PR in Science Mode.
- BS mirror actuator have two modes, HighPower (HP) and LowNoise (LN1) mode. The LowNoise mode is used in Science Mode: it has no shaping filter, and the total resistor is about 230 Ω.
- NE and WE mirror actuators have two modes, LowNoise1 (LN1) and LowNoise2 (LN2). Only the LowNoise2 mode has been used in Science Mode during O2: it has a shaping filter, and the total resistor is about 4500 Ω.

4.2 Which actuators have to be calibrated?

The actuators to be calibrated are the mirror and marionette actuators that are used in Science Mode. In addition, specific data with injections through the NI and WI actuators have been used during O2 to validate the h(t) reconstruction. Hence, the actuators to be calibrated are:

- mirror actuators:
  - NE and WE mirror actuators in LowNoise2 mode,
  - BS mirror actuator in LowNoise1 mode,
  - PR mirror actuator in HighPower mode,
  - NI and WI mirror actuators in HighPower mode.

- marionette actuators:
    - NE, WE and BS marionette actuators.

The response to be calibrated for the h(t) reconstruction is the response from the DSP channels Sc_MIR, MAR as stored in the DAQ to the mirror motion in absolute GPS time. It is hereafter called A_{mir}^{Sc}. Hence their modulus is given in m/V. For some other measurements where we want to apply known external mirror motions into the locked ITF, we must know the response from the CAL_MIR, MAR to the mirror motion. This one is called A_{mir}^{CAL}. These two responses are the same except for a different delay. The delays have been measured every Tuesdays during O2 and are reported[2] in the figure 5 for the WE mirror and marionette channels. They are the same for all the mirrors on one side and for all the marionette on the other side (see appendix G). There values are reported in the table 2. In the following, they are noted τ_{mir} and τ_{mar}.

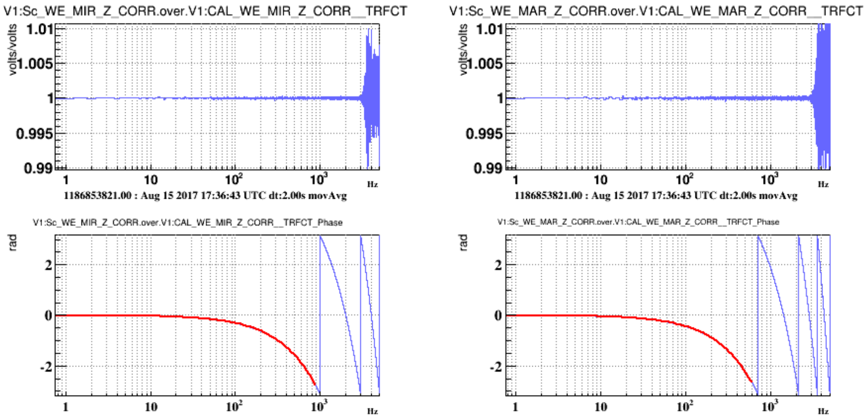

Figure 5: Measurement of the delay from the CAL_WE to the Sc_WE channels for the WE mirror and marionettes.

For h(t) reconstruction, the actuators must be calibrated in the frequency range where the control signals are not negligible: from 10 Hz up to a few about 1 kHz for the mirror actuators, and up to about 50 Hz for the marionette actuators. Extending the calibration a bit higher can be useful to inject known signals at high frequency and compare them to the reconstructed h(t) channel to validate h(t) at high frequency. For O2, we have limited the actuator calibration at 1 kHz.

---

[2] For the WE mirror and marionette actuators, the delays have changed a few days before the run, between 23 and 28 July 2017. This must have happened on 27 July, after the replacement of a faulty DSP board (see logbook entry 38885). Before that date, the delays from CAL to Sc channels were 600 µs and 700 µs for the mirrors and marionettes channels respectively.

Actuator	Mirror actuators	Marionette actuators
Delay (µs)	$\tau_{mir} = 500$	$\tau_{mar} = 700$

Table 2: Summary of the delay from the CAL channels generated in the real-time PC and the corresponding Sc channels sent to the DAQ by the actuator DSP.

4.3 Calibration procedure

The calibration of the different actuators cannot be done in a single measurement. The different steps of overall procedure is shown in figure 6. Some more details about the measurements themselves are given in the following sections.

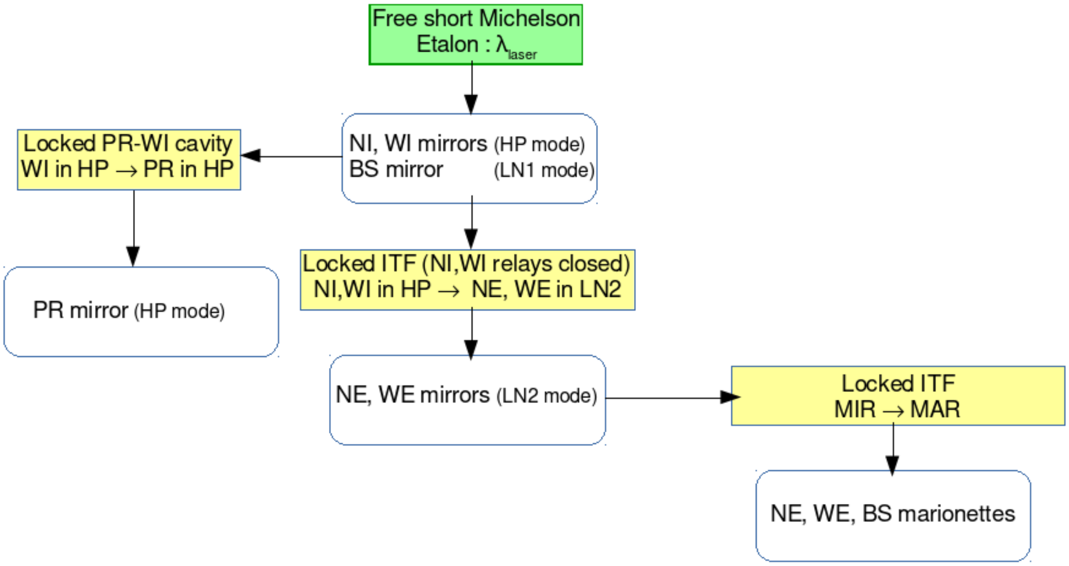

Figure 6: Overview of the mirror and marionette calibration procedure. The filled areas indicate the types of measurements while the empty areas indicate the calibrated actuators.

The Advanced Virgo O2 calibration is based on data in free swinging short Michelson configuration. The short Michelson differential arm length ΔL is reconstructed using the DC and demodulated signals of the B1p photodiode at the interferometer output port. This method uses the main Virgo laser wavelength (1064 nm) as length etalon. Applying sine excitations to the mirrors and looking at their effect in the reconstructed ΔL channel, we can estimate the NI, WI and BS mirror actuator responses.

The following steps are all transfers of the known actuator response to the other actuator responses to be calibrated. With the full interferometer (ITF) locked, one can compare the effect of known motions of the NI and WI mirrors on the dark fringe power to the effect of unknown motions of the NE and WE mirrors: this comparison permits to estimate the NE and WE mirror actuator responses. Similarly, comparing the effect of a known mirror motion and the effect of an unknown marionette motion on the dark fringe power allows to estimate the marionette actuator responses. Finally, locking the cavity PR-BS-WI, the effect of the known WI motion to the effect of the unknown PR motion on the error signal permits to estimate the PR actuation response.

These measurements and the obtained actuation responses are described in the following sections.

5 Calibration of NI, WI, BS mirror actuators: free swinging Michelson

The first step of the calibration is the estimation of the NI, WI and BS mirror actuators responses (A^{Sc}_{mir}) in free swinging short Michelson data, using the laser wavelength as length etalon: $1064.0 \pm 0,1\,\mathrm{nm}$.

5.1 Calibration data and analysis

The ITF is put in the short free swinging Michelson: the PR, NE and WE mirrors are misaligned, and the longitudinal controls of the BS, NI and WI mirrors are switched off. The NI and WI actuators are in HighPower mode. The mode of the BS actuator can be choosen (HighPower or LowNoise). It was always set to LowNoise for the O2 calibration measurements.

The non-linear reconstruction method described in notes [4] and [5] is used to reconstruct the short Michelson differential arm length ΔL as a time series. The photodiode signals used for this reconstruction are $SDB2\_B1p\_DC$ and $SDB2\_B1p\_6MHz\_I$. They are shown in the figure 7(a). The optical responses from the mirror motions to the power variation are flat in modulus and the delays are neglected (of the order of 50 ns due to the light speed from the mirror to the photodiode). The response of the photodiode sensing is not corrected for when reconstructing $\Delta L(t)$.

The sensivitity of this measurement is shown in figure 7(b) as the amplitude spectral density of the ΔL time series. It reaches a plateau of about $10^{-13}\,\mathrm{m}/\sqrt{\mathrm{Hz}}$ from a few 10's of hertz. The resonance frequencies of the double pendulum can also be seen around 0.4 Hz and 0.75 Hz.

For the actuator calibration, some sine signals (hereafter called "lines") are injected to the mirror actuators: the signals are generated via the channels CAL_MIR. Since the mirrors are not controlled during this measurement, the channels Sc_MIR also contain only the injected lines. The transfer function from the Sc_MIR time series to the reconstructed ΔL time series is measured at the injected frequencies. The actuation response A^{Sc}_{mir} can be decomposed into two parts: the pendulum mechanical response and the electronic response. In the following, the pendulum response for mirror motion has been approximated by a simplified model: a complex pole at $f_{pend} = 0.6\,\mathrm{Hz}$ with a quality factor $Q = 1000$. The exact pendulum response is different, but the difference is taken into account along with the electronic response when fitting the residuals.

Strong lines (up to few volts) were sent during the weekly O2 calibration measurements. Lines with lower amplitudes (down to $\sim 0.05\,\mathrm{V}$ have also been injected during post-O2 calibration in order to check the actuator response linearity.

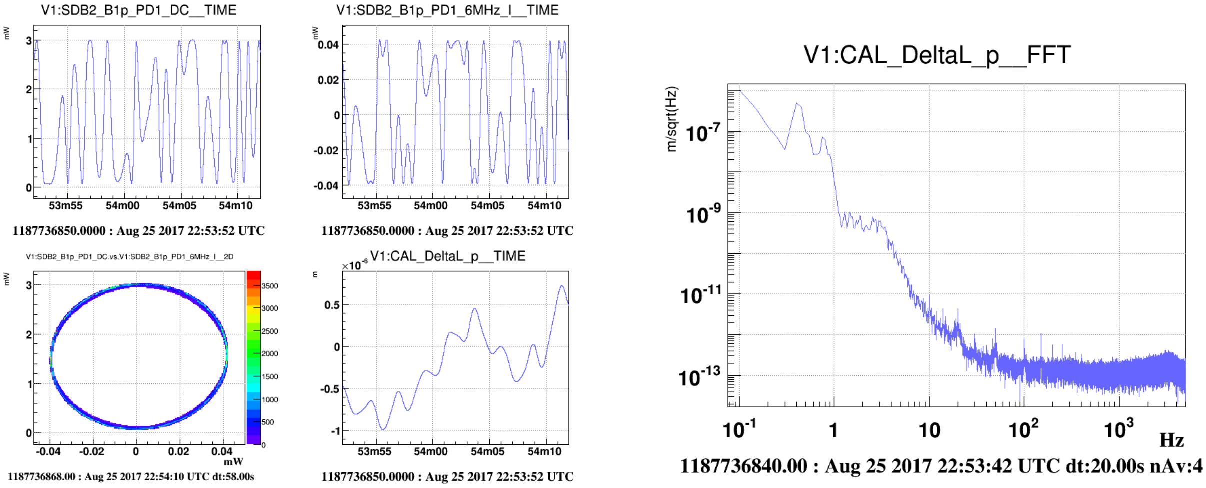

(a) Photodiode signals and reconstructed ΔL (b) Free swinging short Michelson sensitivity

Figure 7: (a) Top: times series of the B1p photodiode channels: DC and in-phase signal demodulated at 6 MHz. Bottom left: ellipse formed by the DC vs I signal. Bottom right: reconstructed time series of ΔL. (b) Sensitivity of the free swinging short Michelson data (amplitude spectral density of the reconstructed ΔL time series.

All the transfer functions measured from end of July to beginning of September are averaged in order to get the final actuation response. The averaged actuation response of WE is shown in section 5.2. Before averaging the data, the stability of the measurements must be validated. This is shown in section 5.3.

For the analysis shown in this note, the transfer functions have been done using FFT length of 10 s, and only the data with coherence higher than 0.70 have been selected for the averaging.

5.2 Measured actuator response

The figure 8(a) shows the measured response of the WE mirror actuation (yet without delay corrections). The modulus is dominated by the $1/f^2$ frequency dependence coming from the pendulum response. This raw response (without delay corrections) is called $A_{mir}^{Sc,raw}$ in the following.

The figure 8(b) shows the same data but normalized by the pendulum model so that the electronics response (and small deviations of the mechanical model from the true response). In the following, we show only the normalized data in order to better see the electronic response to be fit. The normalized data are fit with the expected actuation response shape, and if needed some additionnal poles and zeros to match the measured response. The fit is shown in red in the figure 8(b) and the residuals are shown on the left plots.

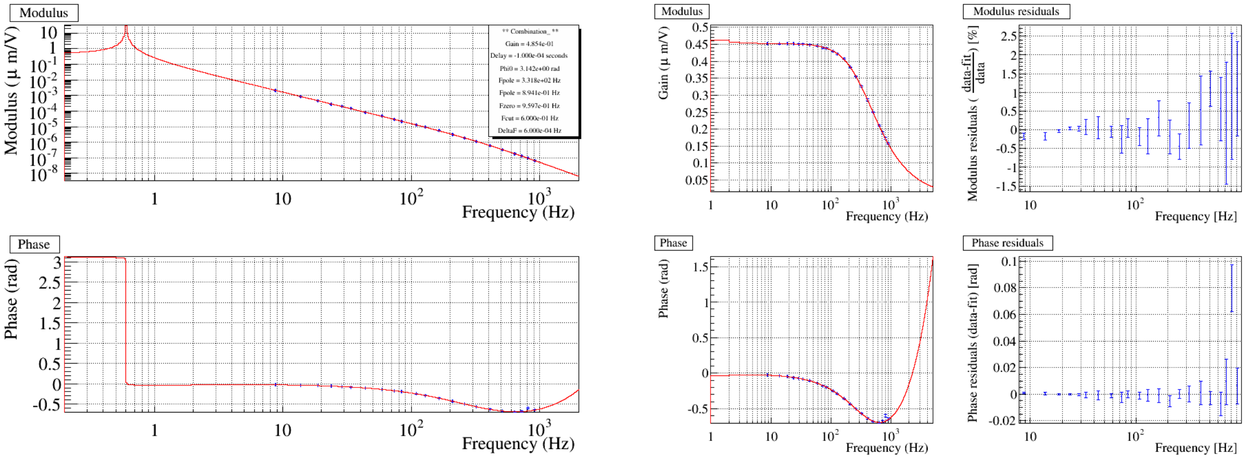

(a) Un-normalized WI actuation response (b) Normalized WI actuation response

Figure 8: Response of the WI mirror actuation (top: modulus, bottom: phase). (a) true values, but phase not corrected for the measurement delays. Above 10 Hz, the modulus is dominated by the $1/f^2$ *frequency dependence of the pendulum response. (b) response normalised by the pendulum mechanical model, still not corrected for the measurement delays. (b-left): data points and fit. (b-right): fit residuals. The pole of the L-R circuit of the coil driver is clearly seen on the modulus.*

The normalisation by the pendulum mechanical response introduces some small systematic uncertainties that will be fixed in future calibration. The normalisation is done by the pendulum response taken at the frequency which is the center of the transfer function bin. This frequency is not exactly the frequency of the injected line. The last digits of the injected line frequencies are $*.27$ and $*.77$, while, for the frequencies used to normalised the transfer functions, they are $*.25$ and $*.75$. This gives a 0.4% bias at 10 Hz, which decreases at high frequencies (0.04% bias at 100 Hz). The effect on the phase is negligible ($\sim 10^{-7}$ rad at 10 Hz).

After averaging all the data, the statistical errors of the measured data are below 1% in modulus and 10 mrad in phase below 500 Hz. From the residuals, the fit matches the data within 2% in modulus and 10 mrad in phase up to 1 kHz.

The raw fit of the WI actuation results in a gain of 0.45234 ± 0.00011 μm/V, a simple pole at 327.5 ± 1.0 Hz and a raw delay of -100.0 ± 1.0 μs. The values of the gain and the pole are consistent with the expected values derived from the nominal electronics design. The expected nominal delay has not yet been estimated.

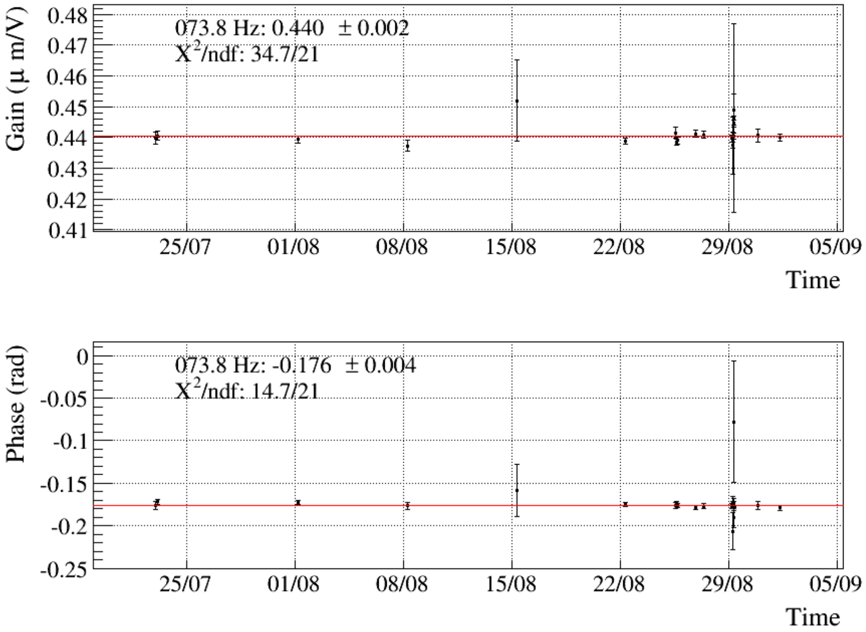

(a) ∼ 72 Hz

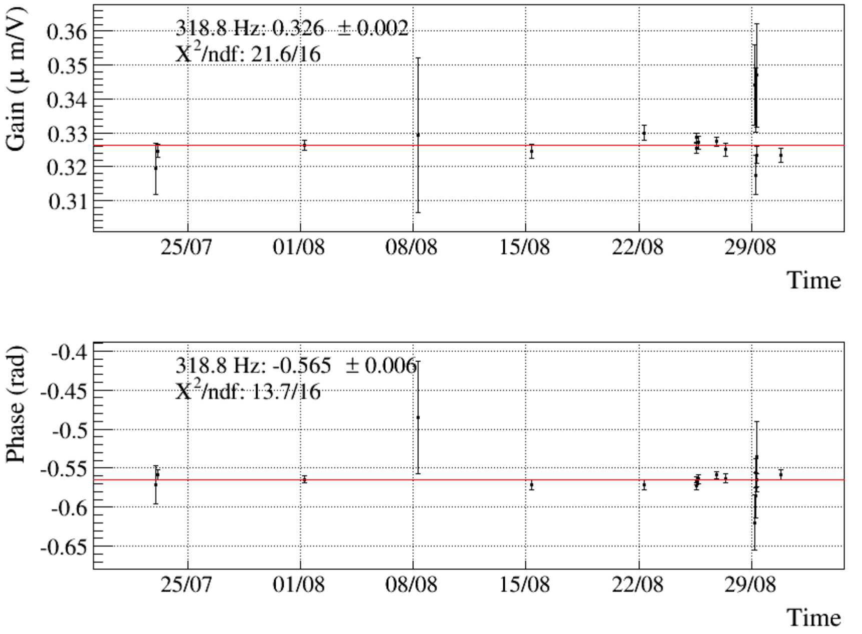

(b) ∼ 317 Hz

Figure 9: Response of the WI mirror actuation as function of time at four different frequencies (Summer 2017).

5.3 Stability of actuator response

5.3.1 Study of the measurement stability vs time

To assess the stability of the actuation response, the time evolution of the modulus and phase measured at a given frequency has been checked. The figure 9 shows the modulus and phase as a function of time at 74 Hz and 319 Hz. The data span from 23rd July to beginning of September 2017. The O2 weekly measurements are seen from 1st to 25th August. Then a lot of post-O2 measurements were added. The first series, on 26th to 27th August, are exactly the same measurements than the ones done during O2. During the measurements done from 29th August, the set of lines and their amplitudes were varied.

The average values are also shown as the red line on the figures, and its $\chi^2/ndof$ is given. This has been done for the 22 injected frequencies between ~ 8 to ~ 910 Hz. At low frequency (up to $\sim 300\ Hz$), typical statistical errors on a single measurement are in general better than 0.5% in modulus and 5 mrad in phase. They increase at higher frequency, reaching 4% and 40 mrad in modulus and phase at 900 Hz. In the example shown here, the response is consistent with a stable behavior in both modulus and phase. Hence the data can be averaged. The statistical error on the averaged modulus and phases are lower than 2% and 20 mrad over the whole frequency band. Some more plots are given in appendix (see figure 29).

5.3.2 Estimation of the systematic uncertainties from time variations

In order to asses the stability at all the measured frequencies, the χ^2 probability of the fits by a constant have been reported in the figure 10(a). In this note, we take as threshold a probability of 5% to answer the question *are the data compatible with a constant as function of time?*: the data are compatible with this hypothesis when the probability is higher than 5%. The first plot shows that all the modulus data measured at frequencies higher than 80 Hz are compatible with a constant as function of time, but some time variations arise at lower frequency (red squares). And all the measured phase data are compatible with constants (blue triangles).

In order to estimate the level of variations, the following method has been processed: increasing systematic errors have been added to the statistical errors and the modified data have been fit until the χ^2 probability is higher than the 5% threshold. Both the initial statistical error of the average and its linear sum with the estimated systematic uncertainties are reported in the figures 10(b) and 10(c) for the modulus and the phase data and for all the measured frequencies. For the modulus, it was needed to add systematic errors only at low frequency, with maximum systematic uncertainty lower than 0.4%. The sum of both stat. and syst. uncertainties is lower than 0.4% up to 500 Hz. No systematic errors are found for the phase since the data are compatible with constant within statistical errors, with stat. errors lower than 3 mrad up to 500 Hz.

As a consequence, we have proceeded with averaging the data to get the overall actuation

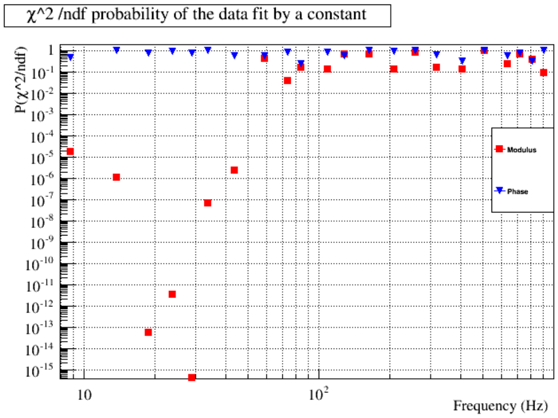

(a) χ^2 probabilities

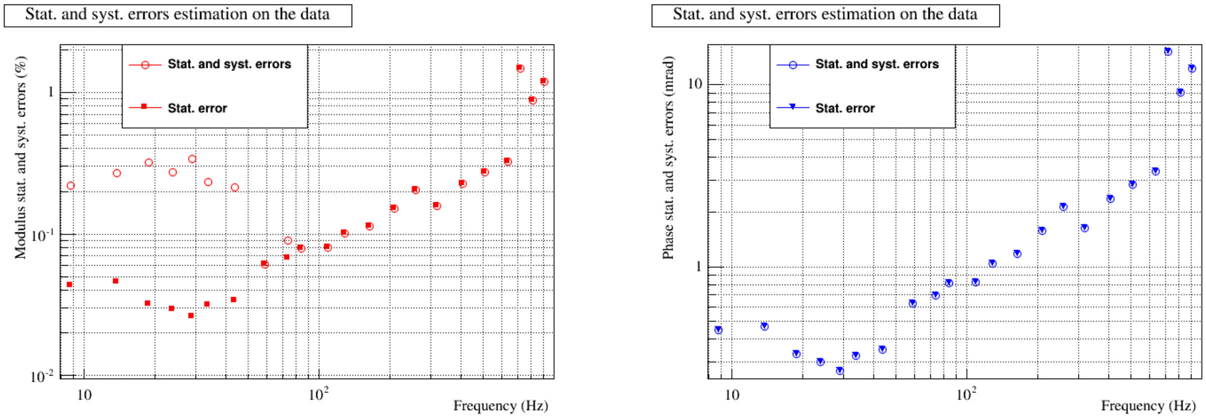

(b) Estimated systematics uncertainties on the modulus (c) Estimated systematics uncertainties on the phase

Figure 10: Estimation of the systematic errors coming from time variations of the measurements for the WI actuation response measured in short Michelson data. (a) χ^2 probability of the fit of the data by a constant vs time at every frequencies. (b) modulus statistical errors (filled markers) and (linear) sum of statistical and additional systematic errors to be added in order to get a high enough probability (empty markers). (c) same but for the phase uncertainties.

response describe in the previous section, but with systematic uncertainties of 0.4% on the modulus.

5.3.3 Study of the measurements stability vs amplitude of the injected signal

The figure 11 shows the same data but plotted as function of the amplitude of the injected signal (amplitude of the sum of all the lines injected together). This study could show some non-linearity in the measurements. The injected signals ranged between 0.1 V and close to

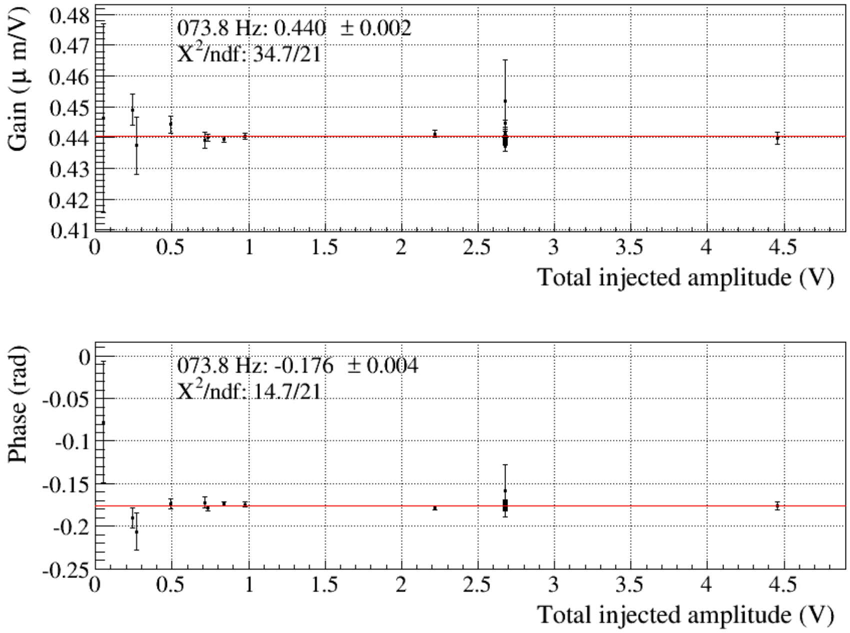

(a) ∼ 72 Hz

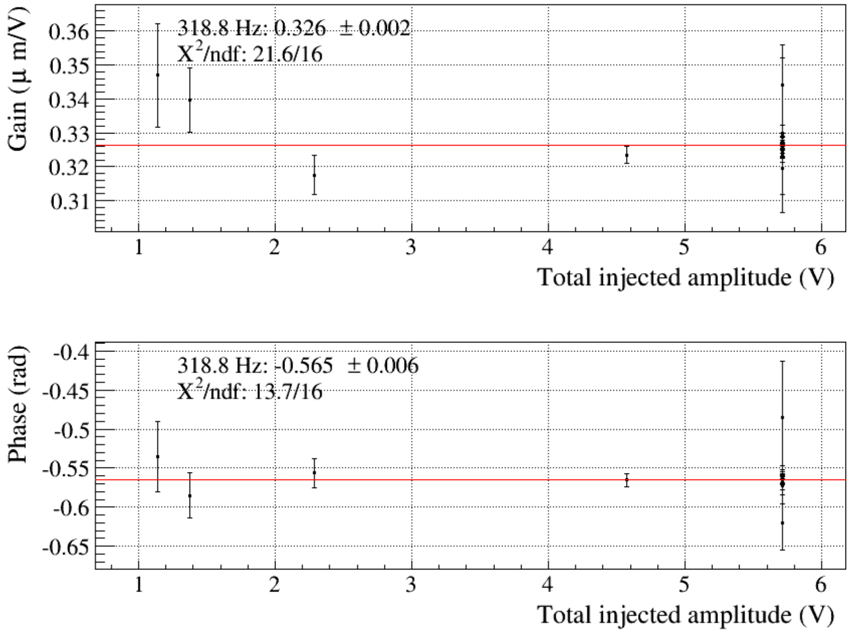

(b) ∼ 317 Hz

Figure 11: Response of the WI mirror actuation as function of the amplitude of the injected signal at four different frequencies.

10 V. Even for the frequencies with the 1% variations, no correlation was found with the signal amplitude.

The similar figures, given at four different frequencies, and for the WI, NI and BS actuators are given in appendix.

6 Calibration of NE and WE mirror actuators: transfer from cavity input to end mirrors

Once the input mirrors, WI and NI, have been calibrated (in HP mode) with the free swinging short Michelson measurements, they are used as reference to calibrate the end mirrors, WE and NE.

6.1 Calibration data and analysis

The ITF is locked in its state called LOW_NOISE_2 (i.e. DC readout, controlling DARM length with the end mirrors, no more with the input mirrors), but with a modification: the NI and WI actuator relays are let closed during the lock acquisition instead of being opened once the controls have been moved to the end mirrors. This allows to inject lines to both the input and end mirrors and to compare their effects on the dark fringe photodiode power.

We can write the effect of the lines on the DARM signal in the frequency domain for both dataset:

$$DARM_{in} = CAL_{in} \times A_{in}^{CAL} \times R_{ITF,in} \quad (1)$$

$$DARM_{end} = CAL_{end} \times A_{end}^{CAL} \times R_{ITF,end} \quad (2)$$

with $CAL_{in,end}$ the signals generated in the real-time PC sent to the input or end mirror actuator as external perturbations, $A_{in,end}$ the actuator response from CAL_MIR to mirror motion ΔL and $R_{ITF,in,end}$ the closed-loop response of the interferometer to a motion of the input or end mirror. From the free Michelson data, we already know the raw response A_{in}^{Sc} from Sc_MIR to mirror motion ΔL. The transfer function from CAL_MIR to Sc_MIR is only a delay as stated in table 2. We call it $D_{in,end}$. We can thus write:

$$DARM_{in} = CAL_{in} \times D_{in} \times A_{in}^{Sc} \times R_{ITF,in} \quad (3)$$

$$DARM_{end} = CAL_{end} \times D_{end} \times A_{end}^{Sc} \times R_{ITF,end} \quad (4)$$

In the data, the time series of $DARM$ and $CAL_{in,end}$ channels are available. We can compute the transfer functions from the injected lines to $DARM$ in both dataset and extract the response A_{end}^{Sc} (from Sc_MIR to ΔL) of the end mirror as:

$$A_{end}^{Sc} = A_{in}^{Sc} \times \frac{DARM_{end}/CAL_{end}}{DARM_{in}/CAL_{in}} \times \frac{R_{ITF,in}}{R_{ITF,end}} \times \frac{D_{in}}{D_{end}} \quad (5)$$

In this section, we use as reference the raw input actuation response $A_{in,raw}^{Sc}$ directly extracted from the free swinging Michelson measurements and not corrected for any delay in the photodiode sensing. We also do not correct for the differences of ITF response to input and end mirror motions nor for the digital delays D. As a consequence, the results shown in this section are:

- the actuation ratio $\frac{DARM_{end}/CAL_{end}}{DARM_{in}/CAL_{in}}$ which is measured directly in the data described above,
- the raw end mirror actuation response $A^{Sc}_{end,raw}$ defined as:

$$A^{Sc}_{end,raw} = A^{Sc}_{in,raw} \times \frac{DARM_{end}/CAL_{end}}{DARM_{in}/CAL_{in}} \tag{6}$$

The corrections for the different delays shown in the above formulae and possible differences between input and end mirrors ITF response are taken into account later, in section 9.

In practice, two consecutive dataset are taken: one with lines injected on the input mirrors for 60 s, and one with lines injected on the end mirrors for 60 s, started about 10 s after the end of the first dataset. When doing this measurement, we assume that the ITF response to mirror motions is stable between both dataset: in particular, we assume that the optical gain is stable. This can be checked by repeating the measurement and checking its stability since, if there are optical gain variations, they should be different and independent for every measurements.

The optical gain can also be estimated at the frequency of the calibration permanent lines in both dataset to validate its stability or to normalize the measured ratio if needed, but this has not be done yet in this analysis.

For the analysis shown in this note, the transfer functions have been done using FFT length of 10 s, and only the data with coherence higher than 0.99 have been selected for the averaging.

6.2 Measured input to end actuation ratio and estimation of end mirror actuator response

The ratio $\frac{DARM_{end}/CAL_{end}}{DARM_{in}/CAL_{in}}$ has been measured every week during O2, and more data have been taken after O2. The post-O2 data has highlighted an issue in some of the weekly measurements: the small injected lines on the input mirrors was close to the DAC quantization level which induced non-linearities. Later post-O2 data have been taken adding a strong high-frequency dithering line on the input mirrors so this issue is fixed.

We still have to carefully check the weekly measurements to remove the dataset with this issue. The current results were computing using only the post-O2 data.

The averaged actuation ratio is shown in figure 12.

6.3 Stability of input to end actuation ratio

As stated above, the current results were computing using only the post-O2 data. We still have to add some weekly O2 data that were not affected by the non-linearity issue to have a longer stability statement.

We took a lot of post-O2 data for this measurement on the night from 5th to 6th September. The data are shown in figure 13: the ratio is compatible with a constant. A lot of different

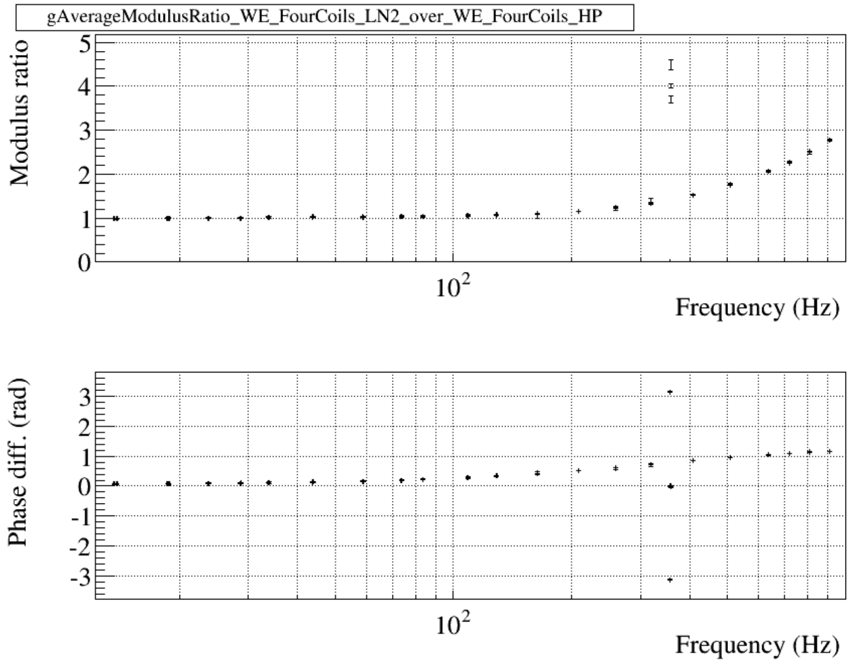

Figure 12: Ratio of the WI and WE actuation response (warning: plot title is wrong).

measurements were done, but they all come from the same night, spanning a time window of 10 hours. Note that they have been taken during three different lock segments.

A more systematic validation of the stability of the measurement has been done, using the same method as described in section 5.3.2. The figures can be found in section D. No significant variation with time was found.

6.4 Raw end mirror actuation response

Combining the raw response of the input mirror known from the free Michelson measurements and the actuation ratio described in this section, we can derive the raw response of the end mirror actuation as shown in equation 6.

The figure 14 shows the electronics part of the raw response $A^{Sc}_{WE,raw}$ of the WE mirror actuator. The expected electronic response is a pole around 40 kHz. Hence, in the 10 Hz to 1 kHz calibration range, we expect a flat response in modulus. The measured response is compatible with this expectation, the modulus being mainly flat, within few percents. This small frequency variation must come from a non perfect tuning of the shaping and un-shaping filters of the actuator.

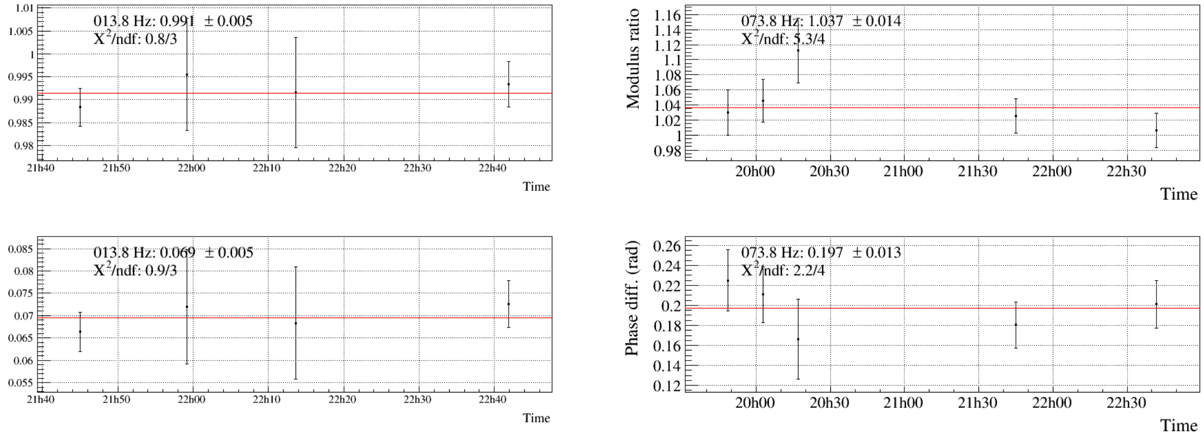

(a) ∼ 12 Hz (b) ∼ 42 Hz

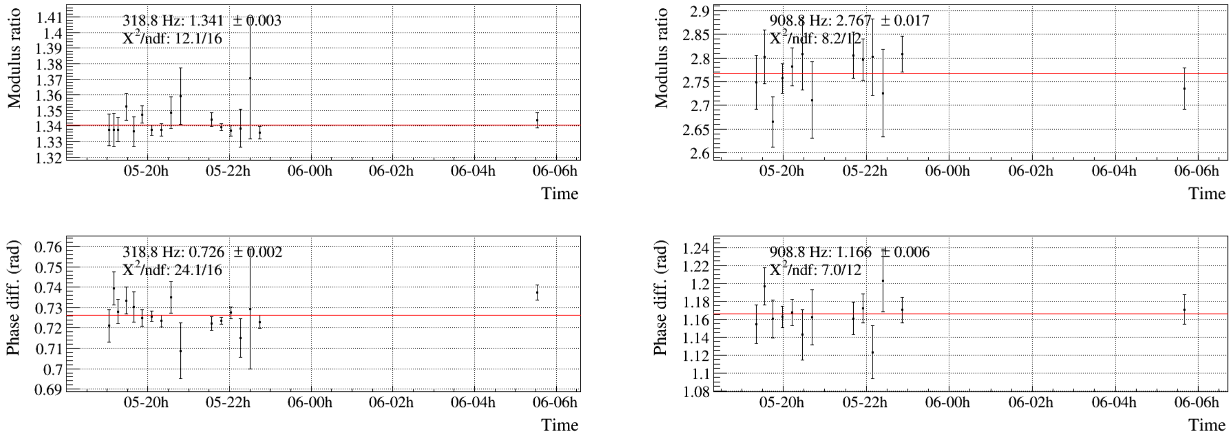

(c) ∼ 317 Hz (d) ∼ 907 Hz

Figure 13: Ratio of the WI and WE actuation response as function of time at four different frequencies.

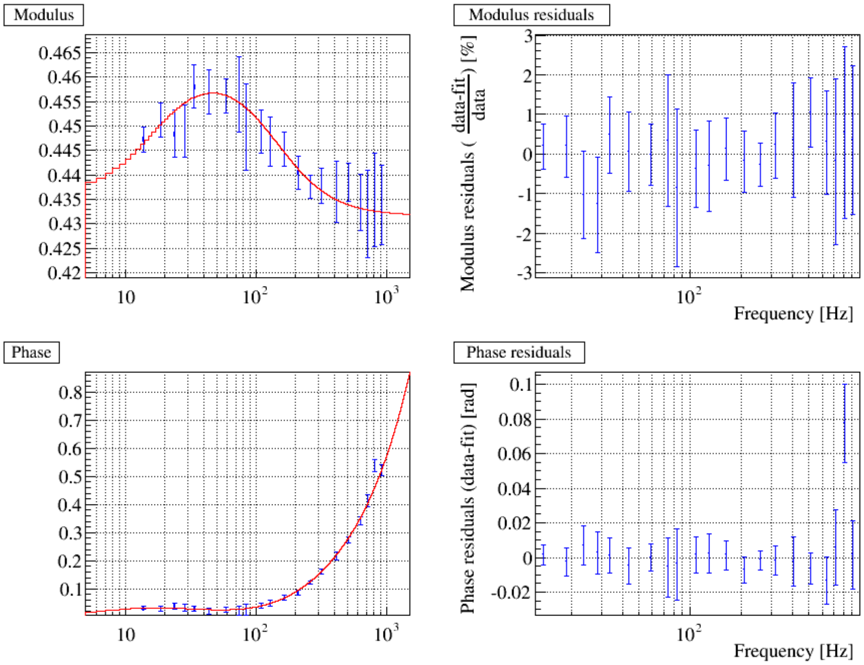

Figure 14: Raw actuation response of the WE mirror, normalised by the pendulum mechanical model.

7 Calibration of NE, WE and BS marionette actuators: transfer from mirror to marionette

7.1 Calibration data and analysis

We can write the effect of the lines on the DARM signal in the frequency domain for both dataset:

$$DARM_{mir} = CAL_{mir} \times A^{CAL}_{mir} \times R_{ITF,end} \tag{7}$$

$$DARM_{mar} = CAL_{mar} \times A^{CAL}_{mar} \times R_{ITF,end} \tag{8}$$

with $CAL_{mir,mar}$ the signals generated in the real-time PC sent to the mirror or marionette actuator as external perturbations, $A^{CAL}_{mir,mar}$ the actuator response from CAL_MIR to mirror motion ΔL and $R_{ITF,end}$ the closed-loop response of the interferometer to a motion of the end mirror. From the combination of the free Michelson data and input to end calibration transfer, we already know the raw response A^{Sc}_{mir} from Sc_MIR to mirror motion ΔL. The transfer function from CAL_MIR to Sc_MIR is only a delay as stated in table 2. We call it $D_{mir,mar}$. We can thus write:

$$DARM_{mir} = CAL_{mir} \times D_{mir} \times A^{Sc}_{mir} \times R_{ITF,end} \tag{9}$$

$$DARM_{mar} = CAL_{mar} \times D_{mar} \times A^{Sc}_{mar} \times R_{ITF,end} \tag{10}$$

In the data, the the time series of $DARM$ and $CAL_{mir,mar}$ channels are available. We can compute the transfer functions from the injected lines to $DARM$ in both dataset and extract the response A^{Sc}_{mar} (from Sc_MAR to ΔL) of the end marionette as:

$$A^{Sc}_{mar} = A^{Sc}_{mir} \times \frac{DARM_{mar}/CAL_{mar}}{DARM_{mir}/CAL_{mir}} \times \frac{D_{mir}}{D_{mar}} \tag{11}$$

In this section, we use as reference the raw mirror actuation response $A^{Sc}_{mir,raw}$ directly extracted from the free swinging Michelson measurements and from the input to end mirror transfer, not corrected for any effects as stated in previous sections. We also do not correct for for the digital delays D. As a consequence, the results shown in this section are:

- the actuation ratio $\frac{DARM_{mar}/CAL_{mar}}{DARM_{mir}/CAL_{mir}}$ which is measured directly in the data described above,
- the raw end mirror actuation response $A^{Sc}_{mar,raw}$ defined as:

$$A^{Sc}_{mar,raw} = A^{Sc}_{mir,raw} \times \frac{DARM_{mar}/CAL_{mar}}{DARM_{mir}/CAL_{mir}} \tag{12}$$

The corrections for the different delays shown in the above formulae and possible differences between input and end mirrors ITF response are taken into account later, in section 9.

In practice, two consecutive dataset are taken: one with lines injected on the mirrors for 60 s, and one with lines injected on the marionette for 60 s, started about 10 s after the end of the first dataset. When doing this measurement, we assume that the ITF response to mirror motions is the same in both dataset: in particular, we assume that the optical gain is stable. This can be checked by repeating the measurement and checking its stability since, if there are optical gain variations, they should be different and independent for every measurements.

The optical gain can also be estimated at the frequency of the calibration permanent lines in both dataset to validate its stability or to normalize the measured ratio if needed, but this has not be done yet in this analysis.

For the analysis shown in this note, the transfer functions have been done using FFT length of 10 s, and only the data with coherence higher than 0.95 have been selected for the averaging.

7.2 Measured mirror to marionette actuation ratio

The ratio $\frac{DARM_{mar}/CAL_{mar}}{DARM_{mir}/CAL_{mir}}$ has been measured every week during O2, and more data have been taken after O2.

The averaged WE actuation ratio is shown in figure 15.

7.3 Stability of mirror to marionette actuation ratio

Measurements were done weekly during O2 and more data were done with different amplitudes and frequencies after the run. The data measured at two frequencies are given as function of time in figure 16: the evolution is not compatible with a constant.

The systematic uncertainties have been estimated with the same method as described in section 5.3.2. The results are shown in the figures 16(c) and 16(d): systematic errors are of the order of 0.2% and 4 mrad on the modulus and the phase respectively.

7.4 Raw marionette actuation response

Combining the raw response of the end mirror known from previous calibration steps and the actuation ratio described in this section, we can derive the raw response of the marionette actuation as shown in equation 12.

The figure 27 shows the electronics part of the raw response $A^{Sc}_{MarWE,raw}$ of the WE marionette actuator.

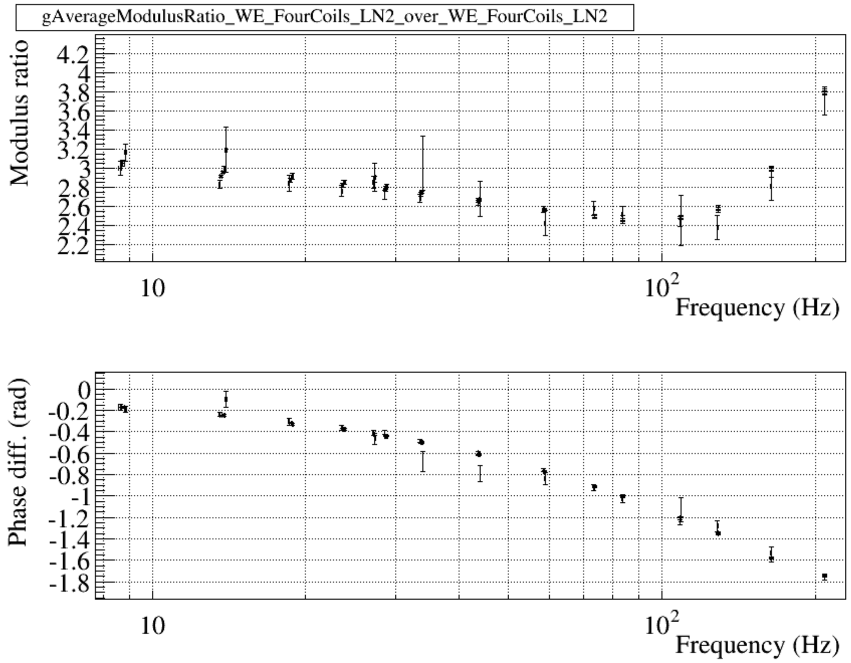

Figure 15: Averaged ratio of the WE mirror to marionette actuation response.

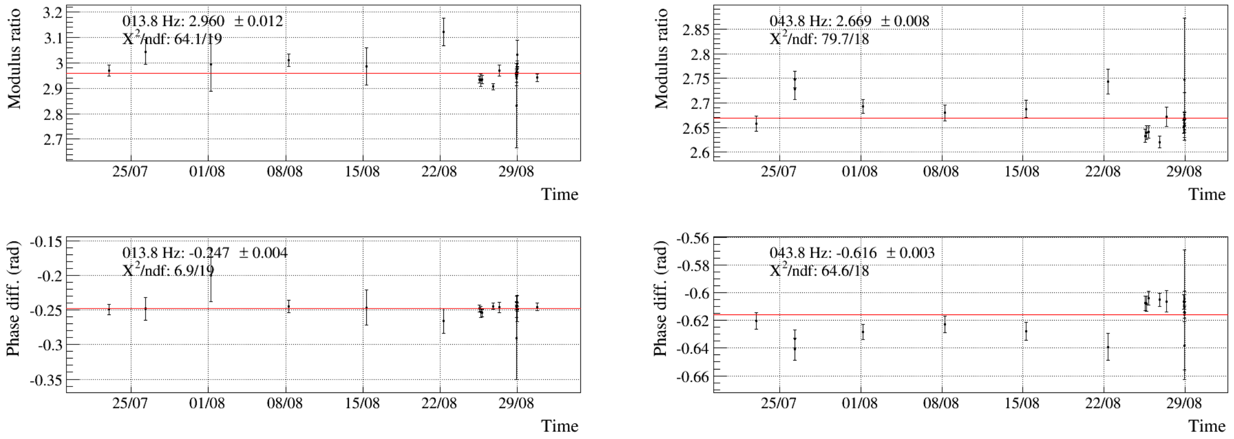

(a) ∼ 12 Hz

(b) ∼ 42 Hz

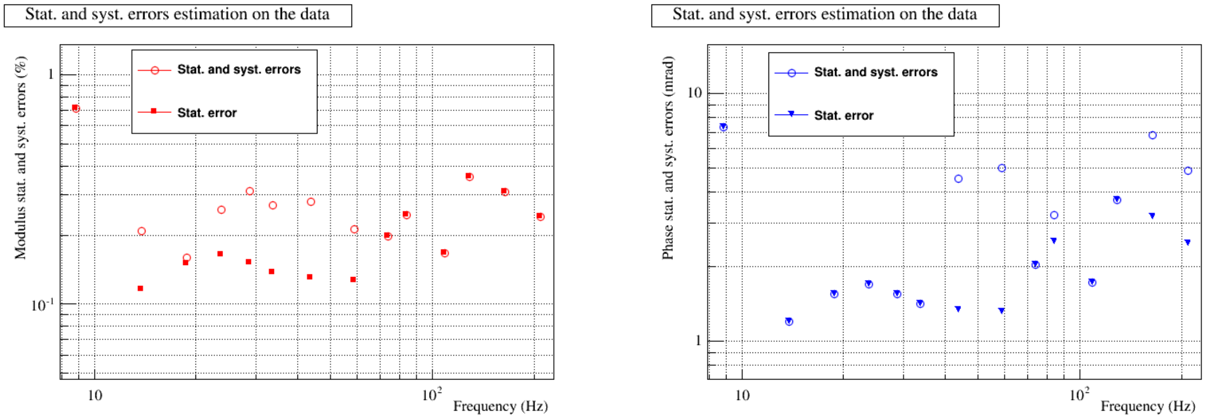

(c) Estimated uncertainties on the modulus

(d) Estimated uncertainties on the phase

Figure 16: Study of WE mirror to marionette actuation ratio stability. Top: ratio of the WE mirror and marionette actuation responses as function of time at two different frequencies. Bottom: estimated statistical and systematic uncertainties as function of frequency for the modulus (c) and the phase (d).

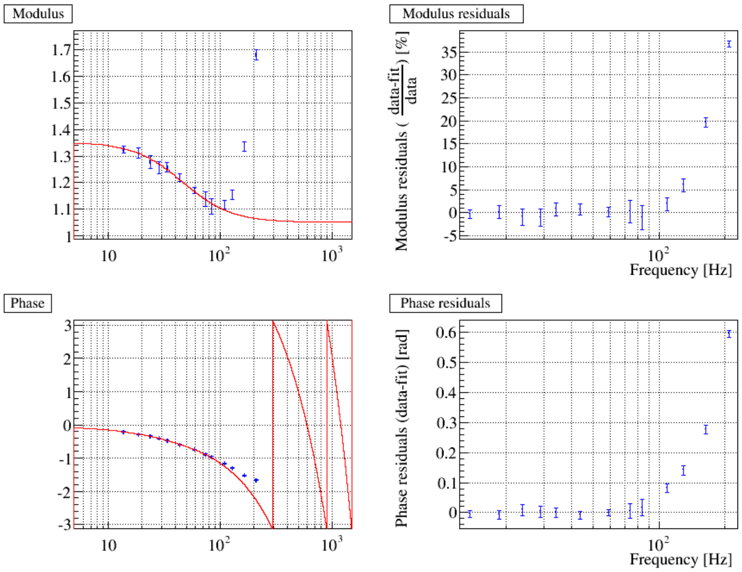

Figure 17: Response of the WE marionette actuation, normalised by the pendulum mechanical response (top: modulus, bottom: phase). The phase has not been corrected for the measurements delays. Left: data points and fit (fit range is 10 to 100 Hz). Right: fit residuals.

8 Calibration of PR mirror actuator: transfer from WI to PR

Once the WI mirror has been calibrated in HP mode with the free swinging short Michelson measurements, it is used as reference to calibrate the PR mirror.

8.1 Calibration data and analysis

Only the cavity made of the mirrors PR-BS-WI is locked, with the PR and WI mirror actuators in HP mode. Lines are injected on the PR mirror and then on the WI mirror. Looking at the effect of the lines on the lock error signal ($PRCL$), we can transfer the calibration from the WI to the PR mirror.

We can write the effect of the lines on the PRCL signal in the frequency domain for both dataset:

$$\begin{aligned} PRCL_{in} &= CAL_{WI} \times A_{WI}^{CAL} \times R_{cavity,WI} && (13) \\ PRCL_{end} &= CAL_{PR} \times A_{PR}^{CAL} \times R_{cavity,PR} && (14) \end{aligned}$$

with $CAL_{WI,PR}$ the signals generated in the real-time PC sent to the WI and PR mirror actuator as external perturbations, $A_{WI,PR}$ the actuator response from CAL_MIR to mirror motion ΔL and $R_{cavity,WI,PR}$ the closed-loop response of the locked cavity to a motion of the different mirrors.

From the free Michelson data, we already know the raw response A_{WI}^{Sc} from Sc_MIR to mirror motion ΔL. The transfer function from CAL_MIR to Sc_MIR is only a delay as stated in table 2. We call it $D_{WI,PR}$. We can thus write:

$$\begin{aligned} PRCL_{WI} &= CAL_{WI} \times D_{WI} \times A_{WI}^{Sc} \times R_{cavity,WI} && (15) \\ PRCL_{PR} &= CAL_{PR} \times D_{PR} \times A_{PR}^{Sc} \times R_{cavity,PR} && (16) \end{aligned}$$

In the data, the time series of $PRCL$ and $CAL_{WI,PR}$ channels are available. We can compute the transfer functions from the injected lines to $PRCL$ in both dataset and extract the response A_{PR}^{Sc} (from Sc_MIR to ΔL) of the PR mirror as:

$$A_{PR}^{Sc} = A_{WI}^{Sc} \times \frac{PRCL_{PR}/CAL_{PR}}{PRCL_{WI}/CAL_{WI}} \times \frac{R_{cavity,WI}}{R_{cavity,PR}} \times \frac{D_{WI}}{D_{PE}} \qquad (17)$$

In this section, we use as reference the raw input actuation response $A_{WI,raw}^{Sc}$ directly extracted from the free swinging Michelson measurements and not corrected for any delay in the photodiode sensing. We also do not correct for the digital delays D. And the response of the cavity to PR and WI mirror motions is the same, so they cancel in the formula. As a consequence, the results shown in this section are:

- the actuation ratio $\frac{PRCL_{PR}/CAL_{PR}}{PRCL_{WI}/CAL_{WI}}$ which is measured directly in the data described above,
- the raw end mirror actuation response $A^{Sc}_{PR,raw}$ defined as:

$$A^{Sc}_{PR,raw} = A^{Sc}_{WI,raw} \times \frac{PRCL_{PR}/CAL_{PR}}{PRCL_{WI}/CAL_{WI}} \tag{18}$$

The corrections for the different delays shown in the above formulae and possible differences between input and end mirrors ITF response are taken into account later, in section 9.

In practice, two consecutive dataset are taken: one with lines injected on the PR mirror for 60 s, and one with lines injected on the WI mirror for 60 s, started about 10 s after the end of the first dataset. When doing this measurement, we assume that the cavity response to mirror motions is stable between both dataset: in particular, we assume that the optical gain is stable. This can be checked by repeating the measurement and checking its stability since, if there are optical gain variations, they should be different and independent for every measurements.

For the analysis shown in this note, the transfer functions have been done using FFT length of 10 s, and only the data with coherence higher than 0.90 have been selected for the averaging.

8.2 Measured actuator response

The ratio $\frac{PRCL_{PR}/CAL_{PR}}{PRCL_{WI}/CAL_{WI}}$ has been measured every week during O2, and more data have been taken after O2.

The averaged actuation ratio is shown in figure 18.

8.3 Stability of actuator response

The figures of the stability of the measurements during O2 and post-O2 data are shown in appendix F. The same method as described in section 5.3.2 has been used. No variation with time larger than 0.3% was found.

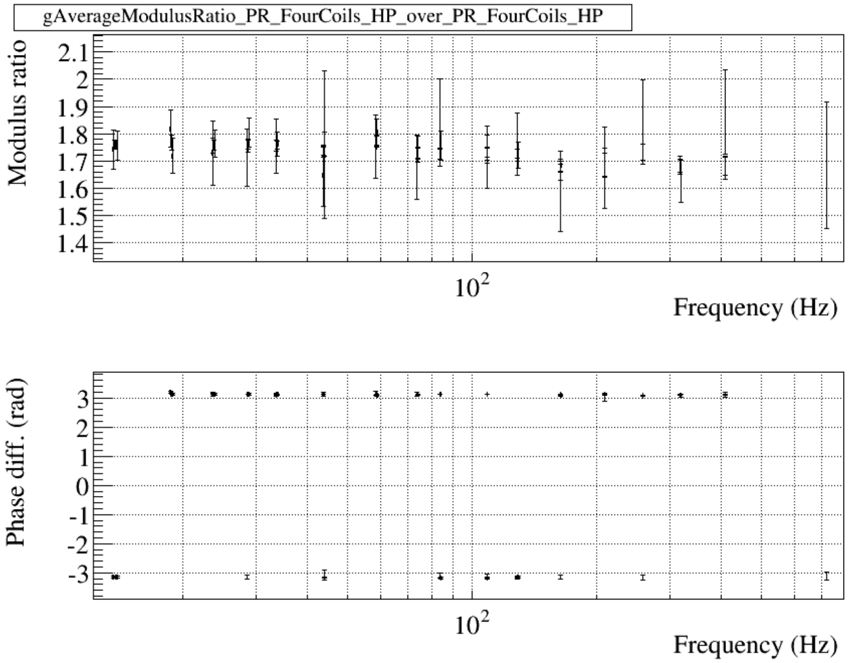

Figure 18: Ratio of the WI and PR actuation response.

9 Estimation of the delays from control signal to mirror motion

9.1 From raw delays to actuation delays

9.1.1 Free swinging Michelson data

For the actuation response measured in free swinging Michelson data, the response is estimated from Sc_MIR channel to the reconstructed ΔL channel. The path between them includes (i) the actuation response itself, (ii) the ITF response, (iii) the B1p photodiode readout and (iv) the reconstruction processing:

- For the short free swinging Michelson configuration, the ITF response from the mirror motion to the dark fringe power is flat in modulus and the delay is negligible (propagation along about 20 meters).

- The B1p photodiode readout is flat in modulus but introduces a delay. The delay from the power reaching the photodiode at a given GPS time to the B1p DC channel stored in the frames has been measured to $\tau_{B1p} = 140 \pm 4$ µs (see section 3).

- The photodiode signals used for this reconstruction are $SDB2\_B1p\_DC$ and

$SDB2\_B1p\_6MHz\_I$. The signal $SDB2\_B1p\_6MHz\_I$ is sampled at 10 kHz while the signal $SDB2\_B1p\_DC$ is sampled at 20 kHz. For the reconstruction, both signals must be at the same frequency. Hence the $SDB2\_B1p\_DC$ signal has been low-pass filtered (6th order Butterworth filter at $f_0 = 10$ kHz) and decimated down to 10 kHz, using Fd software tools, to provide the new input to the reconstruction:
$SDB2\_B1p\_DC\_10000Hz$. Note that the cut-off of the 6th order Butterworth filter was too high to prevent aliasing. The delay from the DC channel to the $DC\_10000Hz$ channel is null: 50 µs from the filter and −50 µs from the decimation.

In total, the actuation response of the NI, WI and BS mirrors can be estimated from the raw actuation response measured in free swinging Michelson subtracting to the raw response this extra-delay of τ_{B1p}:

$$A^{Sc}_{mir(NI,WI,BS)} = \frac{A^{Sc}_{mir(NI,WI,BS),raw}}{\mathrm{e}^{-j\times 2\pi f\tau_{B1p}}} \tag{19}$$

9.1.2 Input to end calibration transfer

From equations 5 and 6, one can derive the actuation response of NE and WE mirror actuators from the actuation response of the raw responses shown in previous sections:

$$A^{Sc}_{mir(NE,WE)} = A^{Sc}_{mir(NE,WE),raw} \times \frac{1}{\mathrm{e}^{-j\times 2\pi f\tau_{B1p}}} \times \frac{R_{ITF,in}}{R_{ITF,end}} \times \frac{\mathrm{e}^{-j\times 2\pi f\tau_{in}}}{\mathrm{e}^{-j\times 2\pi f\tau_{end}}} \tag{20}$$

In this process, we assumed that $R_{ITF,end} = R_{ITF,in} \times \mathrm{e}^{-j\times 2\pi f\tau_{arm}}$ with $\tau_{arm} = 10$ µs the light propagation time in the arm. In addition, a difference in modulus is expected since the motion of the end mirror modifies only the DARM degree of freedom while a motion of the input mirror modifies DARM both other MICH and PRCL degrees of freedom. Simulations have shown that the difference is of the order of 0.3% that has been neglected in the transfer but included later as systematic errors[3].

9.1.3 Mirror to marionette calibration transfer

From equations 11 and 12 and from the previous ones, one can derive the actuation response of marionette actuators from the actuation response of the raw responses shown in previous sections:

$$A^{Sc}_{mar(NE,WE)} = A^{Sc}_{mar(NE,WE),raw} \times \frac{1}{\mathrm{e}^{-j\times 2\pi f\tau_{B1p}}} \times \frac{R_{ITF,in}}{R_{ITF,end}} \times \frac{\mathrm{e}^{-j\times 2\pi f\tau_{in}}}{\mathrm{e}^{-j\times 2\pi f\tau_{end}}} \times \frac{\mathrm{e}^{-j\times 2\pi f\tau_{mir}}}{\mathrm{e}^{-j\times 2\pi f\tau_{mar}}} \tag{21}$$

$$A^{Sc}_{mar(BS)} = A^{Sc}_{mar(BS),raw} \times \frac{1}{\mathrm{e}^{-j\times 2\pi f\tau_{B1p}}} \times \frac{\mathrm{e}^{-j\times 2\pi f\tau_{mir}}}{\mathrm{e}^{-j\times 2\pi f\tau_{mar}}} \tag{22}$$

---

[3] It must be possible to make dedicated measurements of this effect comparing the current input to end calibration transfer data with some data doing the transfer locking only the arms. This must be possible only with the end mirror actuation in LN1 mode and only in the 10-20 Hz range due to the lowest sensitivity of the single arm locks.

Note here that the equation is different for the BS marionette since there is no need to compensate for the input to end calibration transfer.

9.1.4 WI to PR mirror calibration transfer

From equations 17, 18 and 19, one can derive the actuation response of the PR mirror from the raw actuation response shown in previous sections:

$$A_{PR}^{Sc} = A_{PR,raw}^{Sc} \times \frac{1}{\mathrm{e}^{-j\times 2\pi f \tau_{B1p}}} \times \frac{\mathrm{e}^{-j\times 2\pi f \tau_{WI}}}{\mathrm{e}^{-j\times 2\pi f \tau_{PR}}} \tag{23}$$

9.2 Results

Since we have neglected the modulus correction of the ratio $\frac{R_{ITF,in}}{R_{ITF,end}}$, all the corrections to be applied are delays. The table 3 gives, for every actuators, the raw delay estimated from the fit of the raw actuation responses A_{raw}^{Sc}, the different delays to be accounted for as described in this section, and the final delay of the actuation response $A_{mar(BS)}^{Sc}$. Using this delay, one can convert the Sc_MIR, MAR channel into the motion of the mirror at absolute GPS time.

Delays	NE mirror	NE mario.	WE mirror	WE mario.	PR mirror	BS mirror	BS mario.
Raw (µs)	-90.2 ± 1.3	1456 ± 75	-92.9 ± 1.5	1676 ± 55	-101.0 ± 8.7	257.4 ± 3.5	1599 ± 48
$\frac{1}{\mathrm{e}^{-j\times 2\pi f \tau_{B1p}}}$	-140 ± 4						
$\frac{R_{ITF,in}}{R_{ITF,end}}$	-10				$-$	$-$	$-$
$\frac{\mathrm{e}^{-j\times 2\pi f \tau_{in}}}{\mathrm{e}^{-j\times 2\pi f \tau_{end}}}$	0				$-$	$-$	$-$
$\frac{\mathrm{e}^{-j\times 2\pi f \tau_{mir}}}{\mathrm{e}^{-j\times 2\pi f \tau_{mar}}}$		-200	$-$	-200	$-$	$-$	-200
Final delay	-240.2 ± 5.3	1106 ± 79	-242.9 ± 5.5	1326 ± 59	-241.0 ± 13	$+117.4 \pm 7.5$	1259 ± 52

Table 3: Corrections applied on the raw actuation response to obtain the final actuation response, from Sc channel to ΔL.

10 Summary of the actuation models and uncertainties

10.1 Actuation models

The following tables summarize the fit of the measured actuation response that are shown in the figures of appendices A and B. Tables 4 and 5 give the actuation models used in the h(t) reconstruction for the mirrors and marionettes respectively. Table 6 gives the NI and WI actuation models that are used to validate the h(t) reconstruction.

The uncertainties reported in the tables are only the statistical errors output by the fit processed on the data with only statistical error bars. Systematic uncertainties are estimated in the next section.

Some simple poles and zeros have been added in order to improve the fit and better follow some small variations in the actuator responses. In particular two poles and two zeros are used for NE and WE mirror responses in LN2 mode, whose frequencies are close to the shaping filter frequencies. They must be needed since the shaping and un-shaping filter may not be perfectly tuned to compensate completely.

For the NI and WI mirror responses in HP mode, one pole around 300 Hz is the pole expected from the electronics response. The extra low frequency pole and zero improve the residuals, in particular at low frequency. It may compensate for some deviation that we start to see because we use a simplified model for the pendulum response. This will be studied later.

Model		Mirror actuators			
Type	parameters	NE in LN2	WE in LN2	BS in LN1	PR in HP
Gain (µm/V)		0.474 ± 0.002	0.4358 ± 0.0024	1.07977 ± 0.00077	0.7938 ± 0.003
Delay (µs)		-240 ± 1.3	-242.9 ± 1.5	$+117 \pm 3.5$	-241 ± 8.7
1st order pole	f_p (Hz)	17.15 ± 0.4	17.00 ± 0.41	49.4 ± 9	301.4 ± 7
1st order zero	f_0 (Hz)	16.13 ± 0.4	16.00 ± 0.39	50.4 ± 10	–
1st order pole	f_p (Hz)	109.2 ± 3	138.5 ± 4.6	–	–
1st order zero	f_0 (Hz)	117.1 ± 3	148.5 ± 5.0	–	–
2nd order zero	f_0 (Hz)	–	–	877.9 ± 15	–
	Q	–	–	0.668 ± 0.01	–
simple pendulum	f_p (Hz)	0.6			
	Q	1000			

Table 4: Summary of the mirror actuator calibration models useful for h(t) reconstruction: from Sc_MIR channel to mirror motion. Only statistical errors are reported here.

Model		Marionette actuators		
Type	parameters	NE	WE	BS
Gain (μm/V)		1.487 ± 0.011	1.353 ± 0.01	4.645 ± 0.023
Delay (μs)		1106 ± 75	1326 ± 55	1259 ± 48
1st order pole	f_p (Hz)	49.9 ± 3.3	43.6 ± 6	45.1 ± 4
1st order zero	f_0 (Hz)	96.6 ± 13	56.2 ± 10	63.0 ± 7
1st order pole	f_p (Hz)	–	–	–
1st order zero	f_0 (Hz)	–	–	–
2nd order zero	f_0 (Hz)	–	–	–
	Q	–	–	–
two simple pendulum in series	f_p (Hz)	0.6		
	Q	1000		
	f_p (Hz)	0.6		
	Q	1000		

Table 5: Summary of the marionette actuator calibration models useful for h(t) reconstruction: from Sc_MAR channel to mirror motion. Only statistical errors are reported here.

Model		Mirror actuators	
Type	parameters	NI in HP	WI in HP
Gain (µm/V)		0.4998 ± 0.0041	0.4854 ± 0.0025
1st order pole	f_p (Hz)	324.88 ± 0.57	331.78 ± 0.87
1st order pole	f_p (Hz)	0.880 ± 0.060	0.8941 ± 0.0054
1st order zero	f_0 (Hz)	0.957 ± 0.059	0.9597 ± 0.0104
simple pendulum	f_p (Hz)	0.6	
	Q	1000	
Raw delay (µs)		-92.5 ± 0.8	-100.0 ± 1.0
Delay from Sc (µs)		-232.5 ± 0.8	-240.0 ± 1.0
Delay from CAL (µs)		$+267.5 \pm 0.8$	$+260.0 \pm 1.0$

Table 6: Summary of the input mirror actuator calibration models. The raw delay is reminded and the derived delays for the actuation from the Sc channel to ΔL and from the CAL channel to ΔL are given (the delays have been corrected for the B1p photodiode sensing reported in table 1 and additionaly for the CAL to Sc delay reported in table 2). The delay useful for the $h(t)$ validation measurement is the one from CAL. Only statistical errors are reported here.

10.2 Estimated uncertainties

The uncertainties summarized in this section are:

- the systematic uncertainties estimated from time variation of the different measurements,
- the systematic uncertainties estimated from deviations in the fit residuals on the final data,
- some known systematic uncertainties due to approximations in the calibration procedure.

10.2.1 Statistical uncertainties

The statistical uncertainties are estimated for each dataset and every points of the transfer functions from the coherence between the studied channels and the number of averages. We have injected lines at the same frequencies in all the mirrors and marionettes whose calibration is being transferred from one to another, so that we can combine the data directly, without using any intermediate fit of the data. Hence, the data shown in the figures of the sections Aăand B include all the statistical uncertainties, but no systematic uncertainties.

Then, when fitting the data, the fit output the parameters with their associated statistical errors. These values are the ones reported in the tables of the previous section. They are negligible compared to the systematic uncertainties that are estimated below.

10.2.2 Estimation of systematic uncertainties

The estimated systematic uncertainties are summarized in the table 7.

The first set of lines (*Stability vs time*) gives the systematic uncertainties estimated from the time stability studies for every types of measurements. The reported uncertainty is the one that must be added (linearly) to the statistical error so that the measured data are consistant with a constant as function of time, with a χ^2 probability higher than 5% (as described in section 5.3.2).

In the line *Fit residuals*, the uncertainties are estimated looking at the deviations of the actuation fit residuals shown in the figures of sections A and B. Even when there is no significant deviation, we have here put a number with an estimation of the residual width, including there statistical error bars. This is a conservative estimate.

In the line Δf *in normalisation*, the frequency dependent bias introduced by using an approximate frequency when normalising the free Michelson data by the pendulum response model and discussed in section 5.2. is reported.

In the line R_{ITF} *diff (in to end)*, the small difference between the ITF response to a motion of input and end mirrors that has been neglected in the input to end mirror actuation transfer (see section 6) is reported.

Estimations of timing uncertainties coming from either the photodiode sensing or the absolute Virgo timing are also reported.

Finally, a (linear) sum of the different contributions is done and reported in the last line of the table, with different uncertainties estimated for each actuator. Typical systematic errors on the actuator responses are 1% in modulus, few mrad in phase and few µs in timing.

10.2.3 Summary: models and uncertainties

To summarize, the actuation models with their statistical errors are reported in tables 4, 5 and 6. The statistical errors are negligible, except for the timing errors.

The systematic uncertainties are given in the last line of the table 7.

In particular, the total uncertainties on the gain and the pase of the actuation response must be taken from the last lines of table 7, and the total uncertainties on the timing must be taken as the sum of the statistical and systematic uncertainties from the tables.

Source of uncertainty			NE mirror	NE mario.	WE mirror	WE mario.	PR mirror	BS mirror	BS mario.
Systematic errors	Stability vs time	free Mich	0.4% 0		0.4% 0			0.2% 3 mrad	
		in to end	0 0		0 0.5 mrad		– –		
		mir to mar	– –	0.3% 3 mrad	– –	0.2% 4 mrad	– –	– –	0 1 mrad
		WI to PR	– –				0.3% 0	– –	
	Fit residuals		0.5% 5 mrad	2% 10 mrad	0.5% 5 mrad	1% 10 mrad	2% 20 mrad	1% 5 mrad	0.5% 5 mard
	Δf in normalisation		0.2% at 20 Hz and 0.04% at 100 Hz 0						
	R_{ITF} diff (in vs end)		0.3% bias 0				– –		
	Timing (B1p) Timing (GPS)		4 µs <4.5 µs						
	Total systematics (linear sum)		1.4% 5 mrad 4 µs	3.2% 13 mrad 4 µs	1.4% 5.5 mrad 4 µs	2.1% 14.5 mrad 4 µs	2.9% 20 mrad 4 µs	1.4% 8 mrad 4 µs	0.9% 9 mrad 4 µs

Table 7: Summary of the source of systematic uncertainties on the mirror and marionette actuator models. For every sources, the uncertainties on the modulus and on the phase are given in the first and second lines respectively (except for the systematic coming from the B1p timing). The last line gives, for all the actuators, the sum of all the systematic uncertainties reported in this table.

11 Comparison with pre-O2 actuation models

The new actuation models for WE and NE mirrors are compared to the models used for the online h(t) reconstruction during O2. Both are superposed in figure 19 and their residuals are given. Looking in particular at the modulus at the frequency of the calibration lines used to normalise the B1 power in the h(t) reconstruction, they have changed by -3.8% and -5.4% for WE and NE respectively (this number is calculated as: $(G_{online} - G_{new})/G_{online}$).

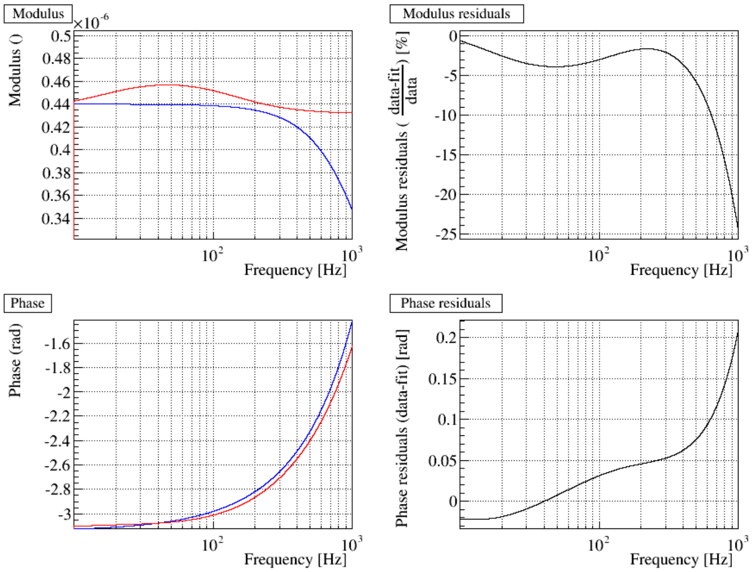

(a) WE mirror actuation

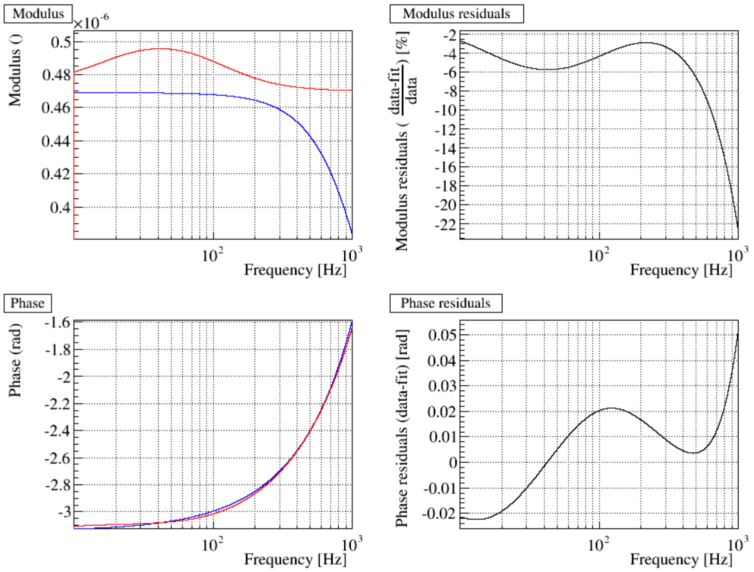

(b) NE mirror actuation

Figure 19: Comparison of the models described in this note to the models used online for h(t) reconstruction during O2, for WE (a) and NE (b) mirror actuators in LN2 mode. Left: modulus (top) and phase (bottom) of the actuation normalised by the pendulum mechanical response. The blue curve is the online mode and the red curve is the updated model from this note. Right: residuals between the two models in modulus (top, $(G_{online} - G_{new})/G_{online}$) and in phase (bottom, $\phi_{online} - \phi_{new}$).

References

[1] B. Mours, L. Rolland, *et al.*, "V1O2Repro1A $h(t)$ reprocessing for Virgo O2 data," *Virgo note*, vol. VIR-0706B-17, Sept. 2017.

[2] B. Mours, L. Rolland, *et al.*, "Check of the DAQ timing during O2," *Virgo note*, vol. VIR-0708B-17, Sept. 2017.

[3] L. Rolland *et al.*, "Stability of the timing system during vsr2," *Virgo note*, vol. VIR-0354A-10, June 2010.

[4] L. Rolland *et al.*, "Mirror motion reconstruction for free swinging Michelson data," *Virgo note*, vol. VIR-0112A-08, Nov. 2008.

[5] L. Rolland, "Free Michelson calibration for Advanced Virgo," *Virgo note*, vol. VIR-0119A-13, Apr. 2013.

A Mirror actuation response: figures

In this appendix, the actuation response normalised by the pendulum mechanical response are shown (from $Sc\_MIR\_Z\_CORR$ channels to mirror motion). For every actuator, the left column gives the data points (modulus and phase) with their statistical errors only, and the fit is plotted on top of the data. The right column gives the fit residuals.

The fit parameters are given in section 10.

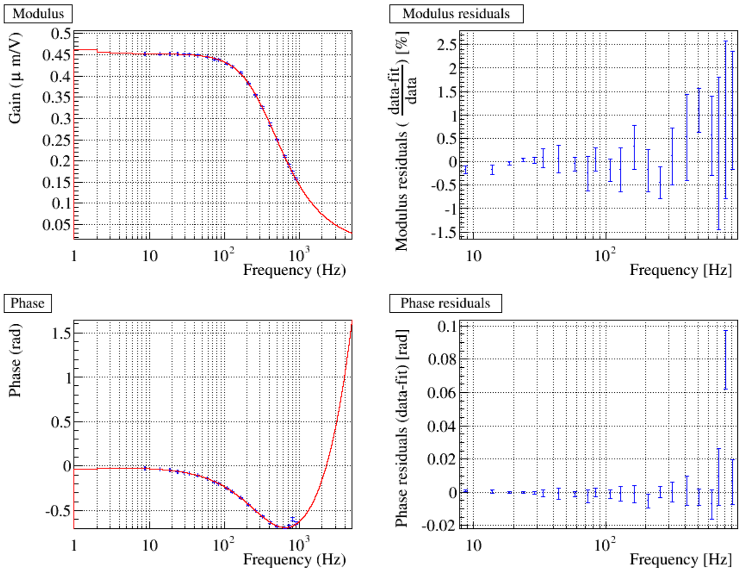

Figure 20: Response of the WI mirror actuation in HP mode, normalised by the pendulum mechanical response (top: modulus, bottom: phase). The phase has not been corrected for the measurements delays. Left: data points and fit. Right: fit residuals.

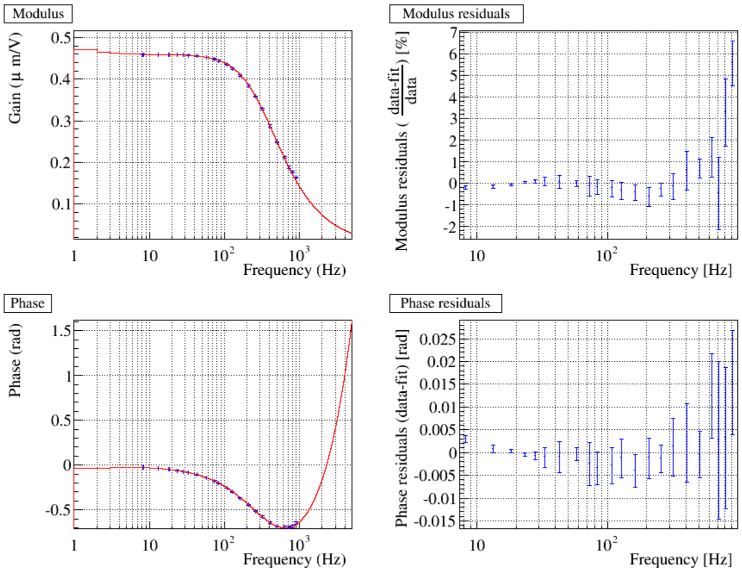

Figure 21: Response of the NI mirror actuation in HP mode, normalised by the pendulum mechanical response (top: modulus, bottom: phase). The phase has not been corrected for the measurements delays. Left: data points and fit. Right: fit residuals.

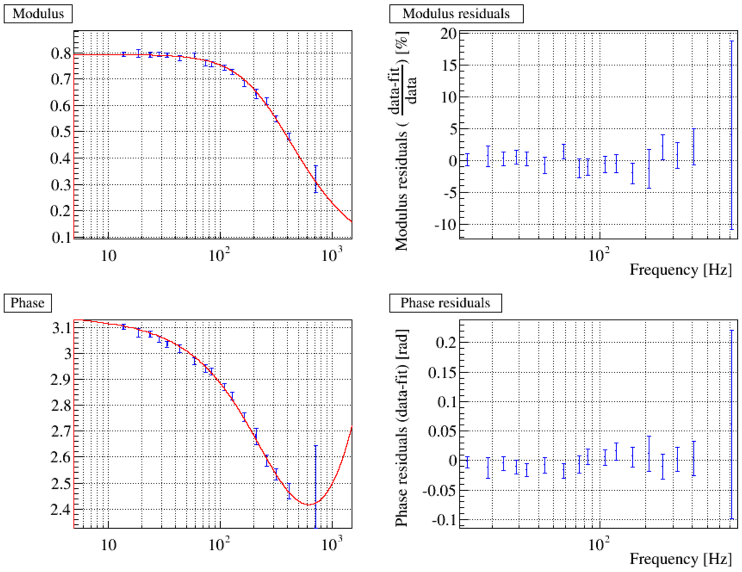

Figure 22: Response of the PR mirror actuation in HP mode, normalised by the pendulum mechanical response (top: modulus, bottom: phase). The phase has not been corrected for the measurements delays. Left: data points and fit. Right: fit residuals.

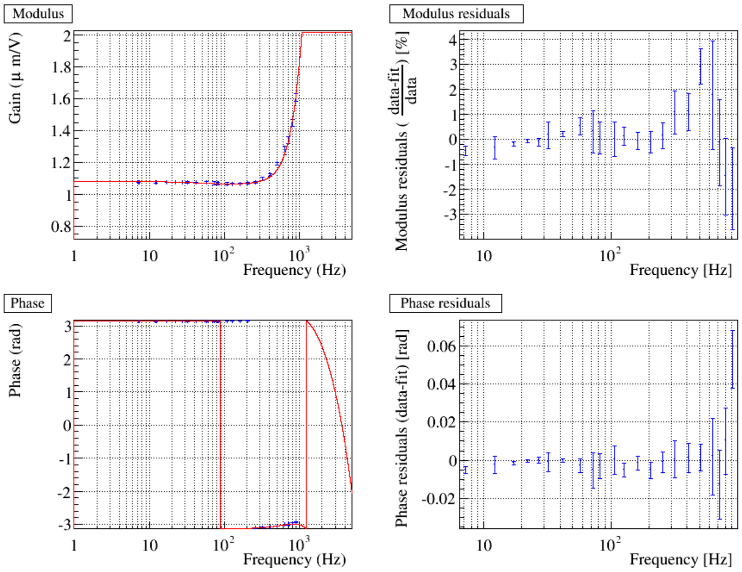

Figure 23: Response of the BS mirror actuation in LN mode, normalised by the pendulum mechanical response (top: modulus, bottom: phase). The phase has not been corrected for the measurements delays. Left: data points and fit. Right: fit residuals.

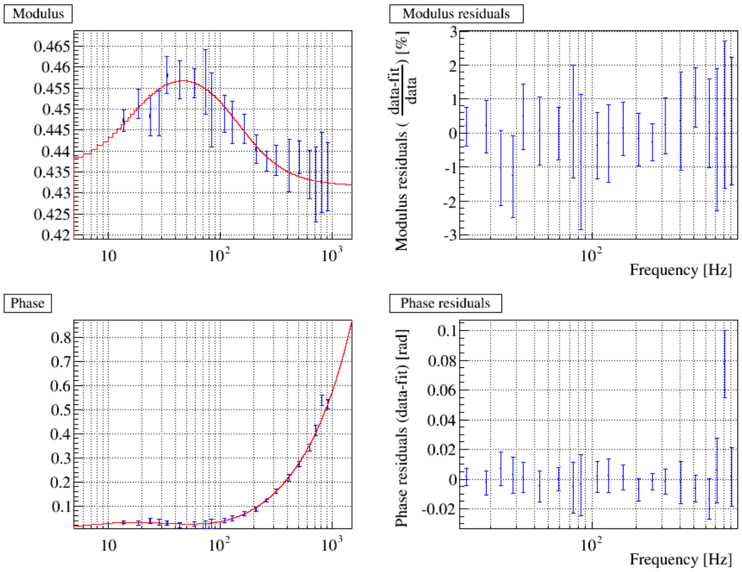

Figure 24: Response of the WE mirror actuation in LN2 mode, normalised by the pendulum mechanical response (top: modulus, bottom: phase). The phase has not been corrected for the measurements delays. Left: data points and fit. Right: fit residuals.

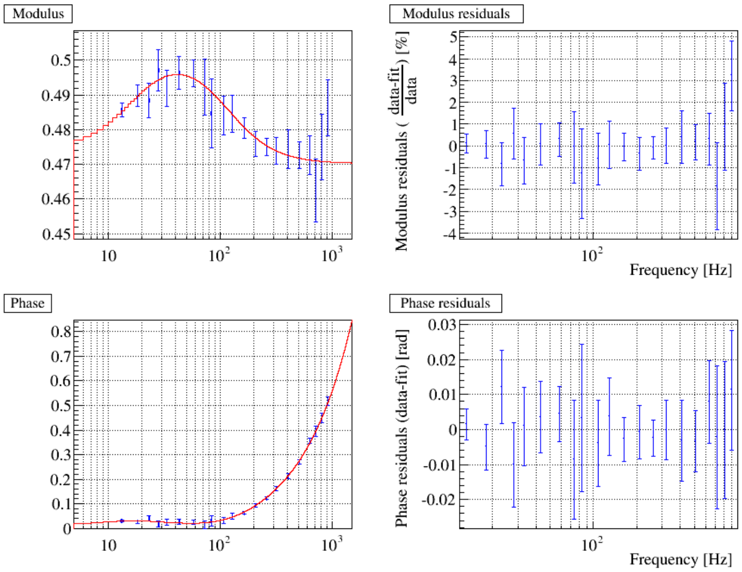

Figure 25: Response of the NE mirror actuation in LN2 mode, normalised by the pendulum mechanical response (top: modulus, bottom: phase). The phase has not been corrected for the measurements delays. Left: data points and fit. Right: fit residuals.

B Marionette actuation response: figures

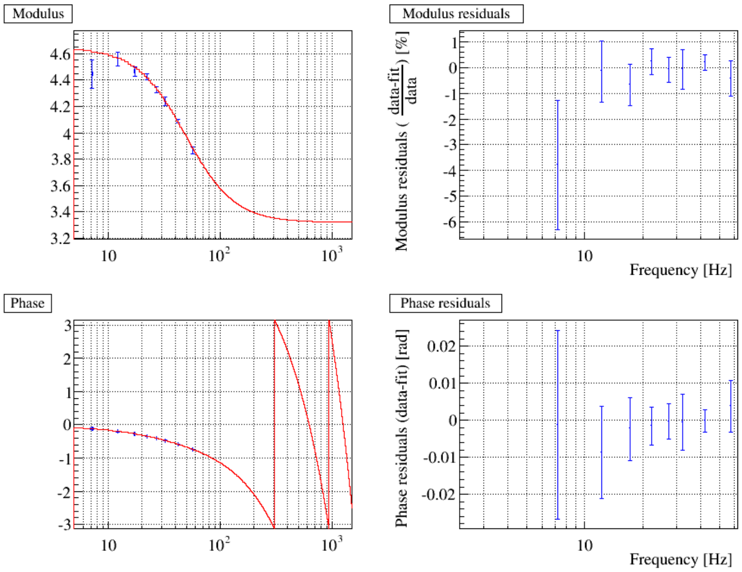

Figure 26: Response of the BS marionette actuation, normalised by the pendulum mechanical response (top: modulus, bottom: phase). The phase has not been corrected for the measurements delays. Left: data points and fit (fit range is 10 to 80 Hz). Right: fit residuals.

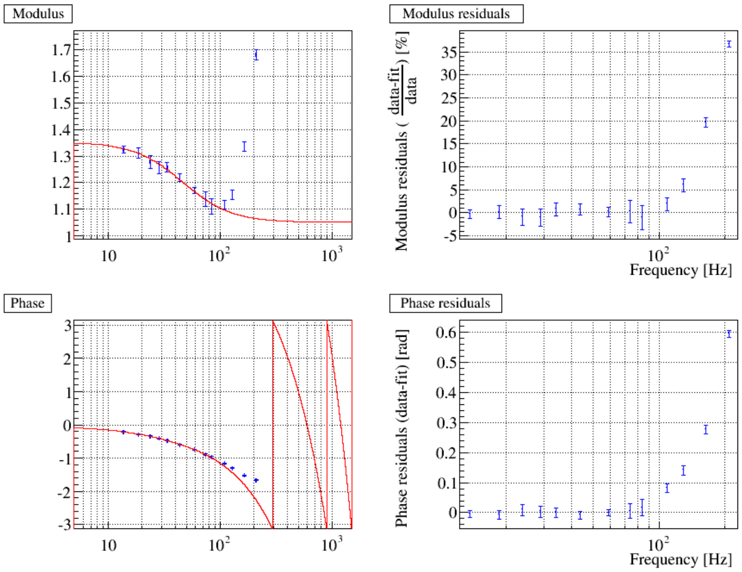

Figure 27: Response of the WE marionette actuation, normalised by the pendulum mechanical response (top: modulus, bottom: phase). The phase has not been corrected for the measurements delays. Left: data points and fit (fit range is 10 to 100 Hz). Right: fit residuals.

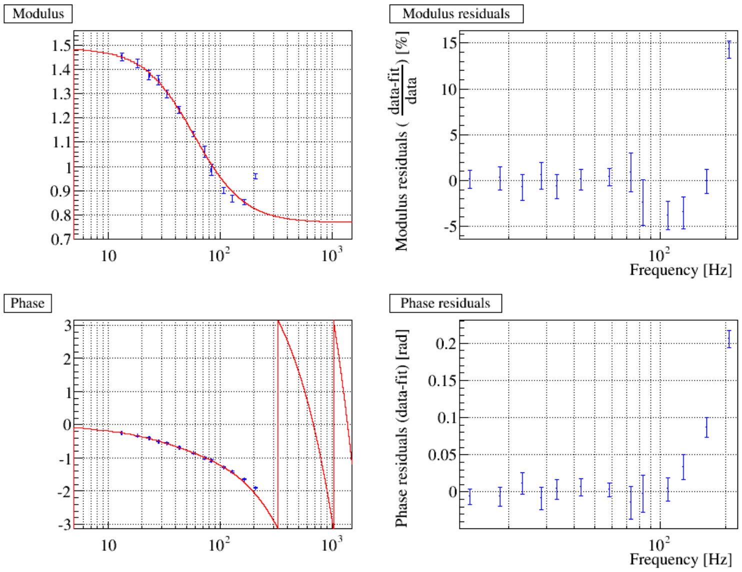

Figure 28: Response of the NE marionette actuation, normalised by the pendulum mechanical response (top: modulus, bottom: phase). The phase has not been corrected for the measurements delays. Left: data points and fit (fit range is 10 to 100 Hz). Right: fit residuals.

C Stability of free swinging Michelson measurements: figures

C.1 WI mirror actuation

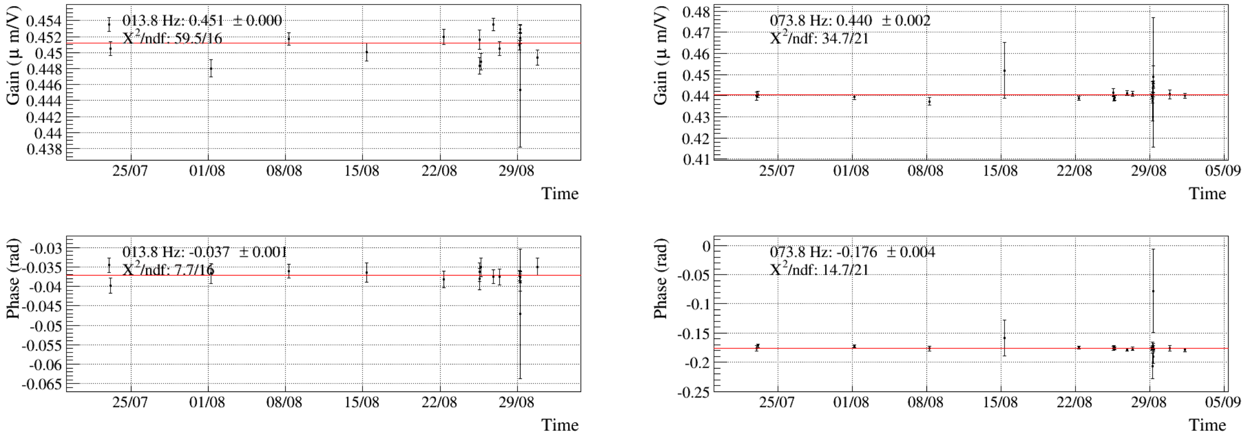

(a) ∼ 12 Hz (b) ∼ 42 Hz

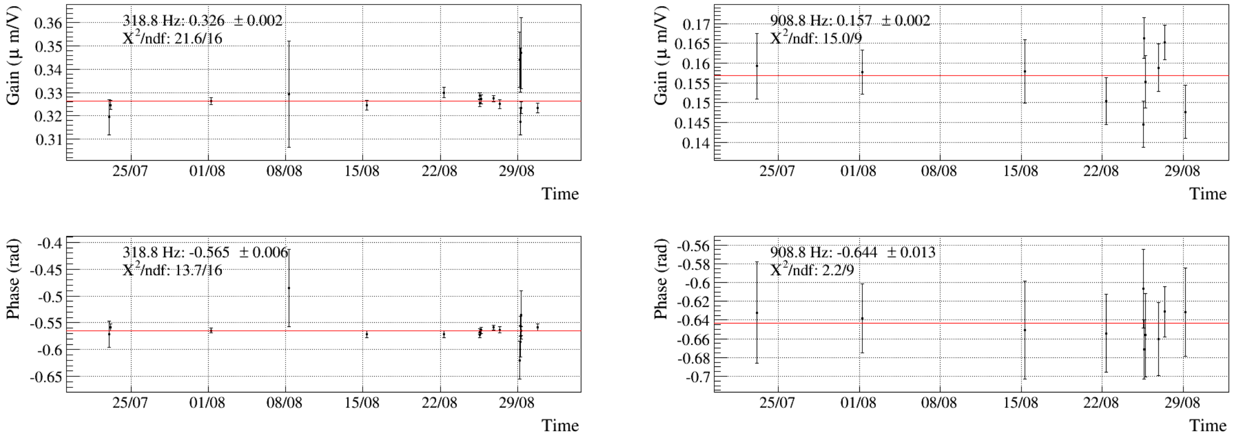

(c) ∼ 317 Hz (d) ∼ 907 Hz

Figure 29: Response of the WI mirror actuation as function of time at four different frequencies.

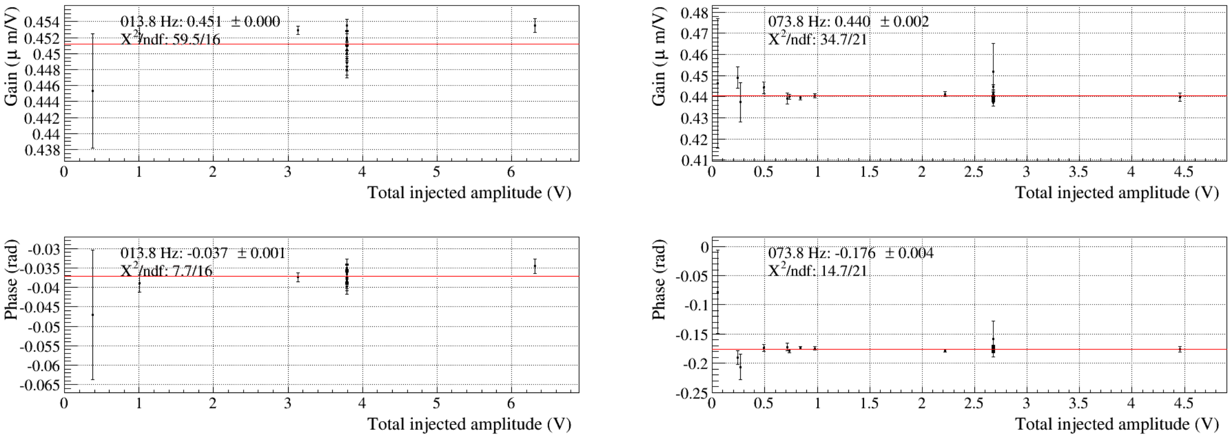

(a) ∼ 12 Hz (b) ∼ 42 Hz

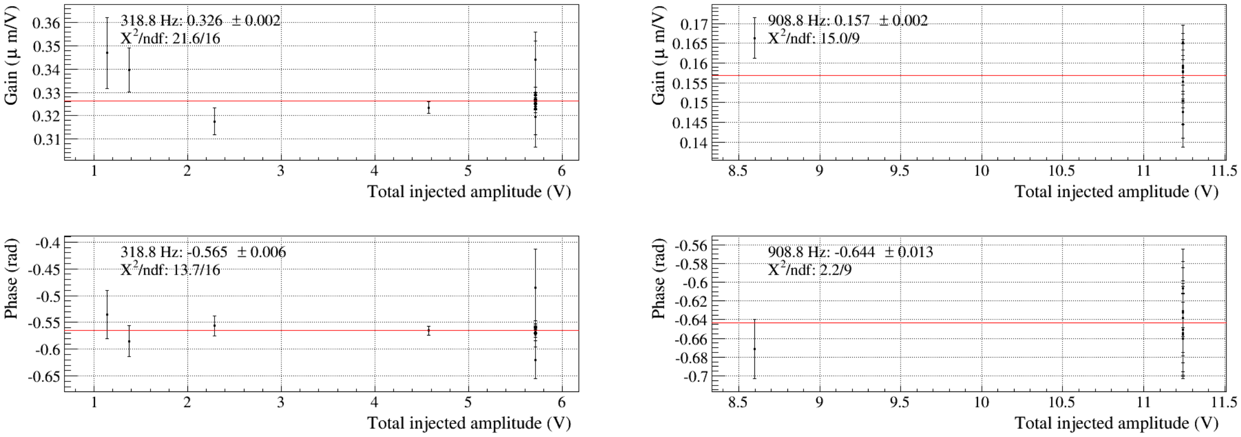

(c) ∼ 317 Hz (d) ∼ 907 Hz

Figure 30: Response of the WI mirror actuation as function of the amplitude of the injected signal at four different frequencies.

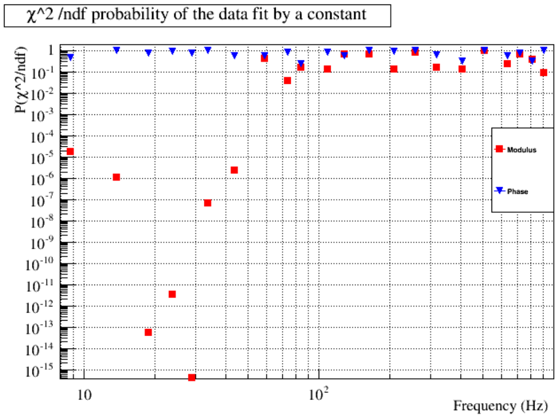

(a) χ^2 probabilities

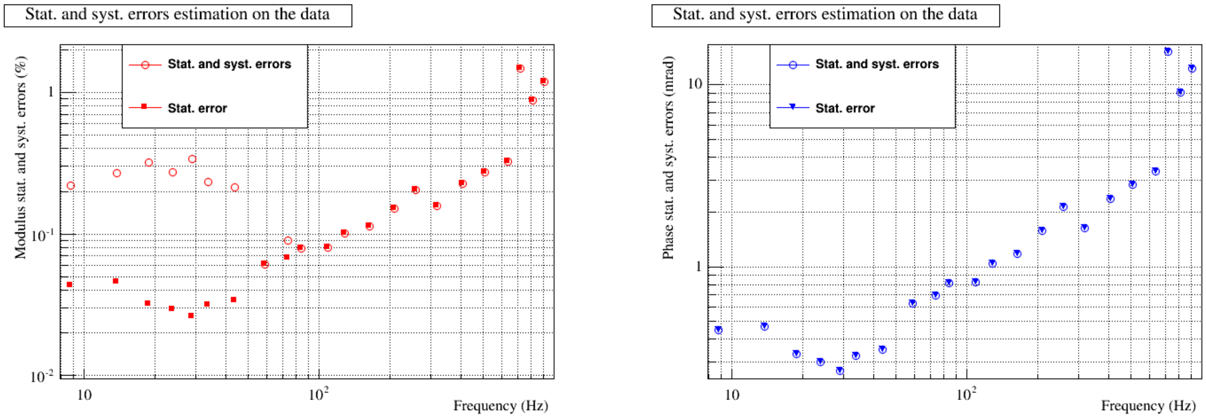

(b) Estimated uncertainties on the modulus (c) Estimated uncertainties on the phase

Figure 31: Estimation of the systematic errors coming from time variations of the measurements for the WI actuation response measured in short Michelson data. (a) χ^2 *probability of the fit of the data by a constant vs time at every frequencies. (b) stat. and sum of stat. and syst. errors to be added in order to have data compatible with a constant in time for the modulus. (c) same for the phase..*

C.2 NI mirror actuation

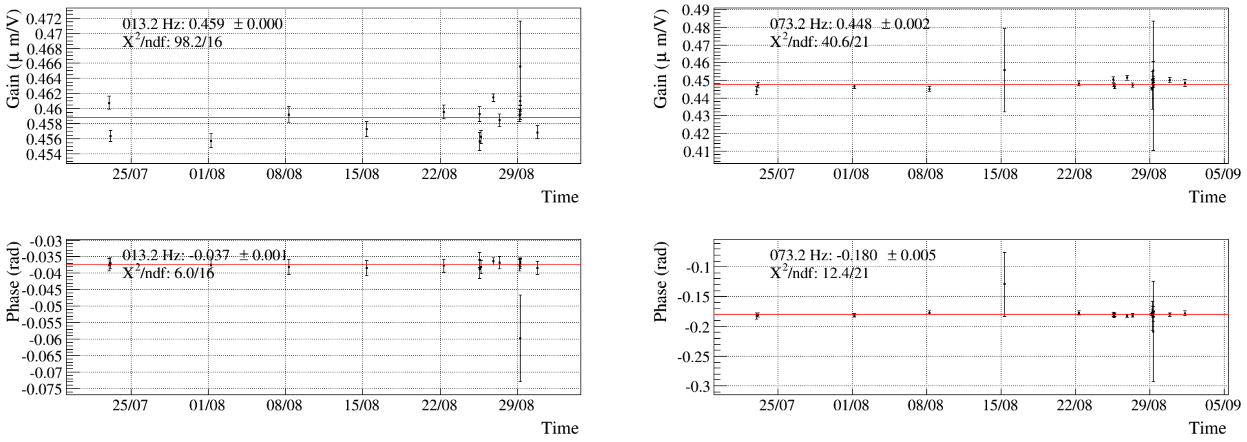

(a) ∼ 12 Hz

(b) ∼ 42 Hz

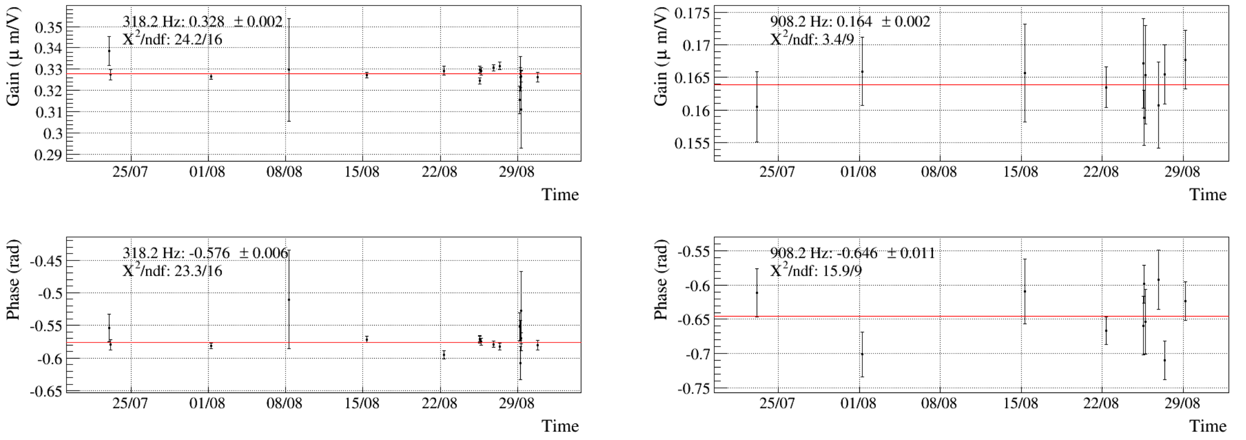

(c) ∼ 317 Hz

(d) ∼ 907 Hz

Figure 32: Response of the NI mirror actuation as function of time at four different frequencies.

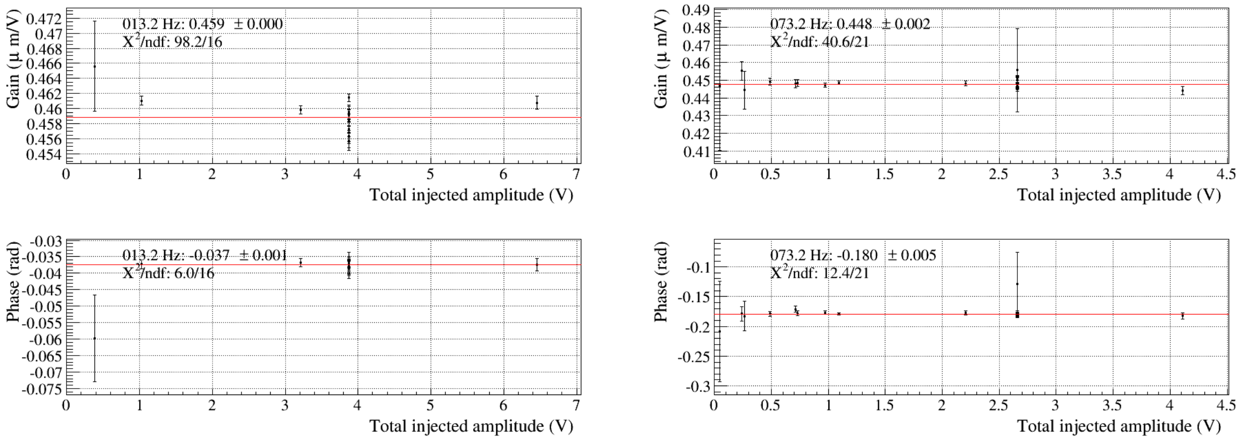

(a) ~ 12 Hz

(b) ~ 42 Hz

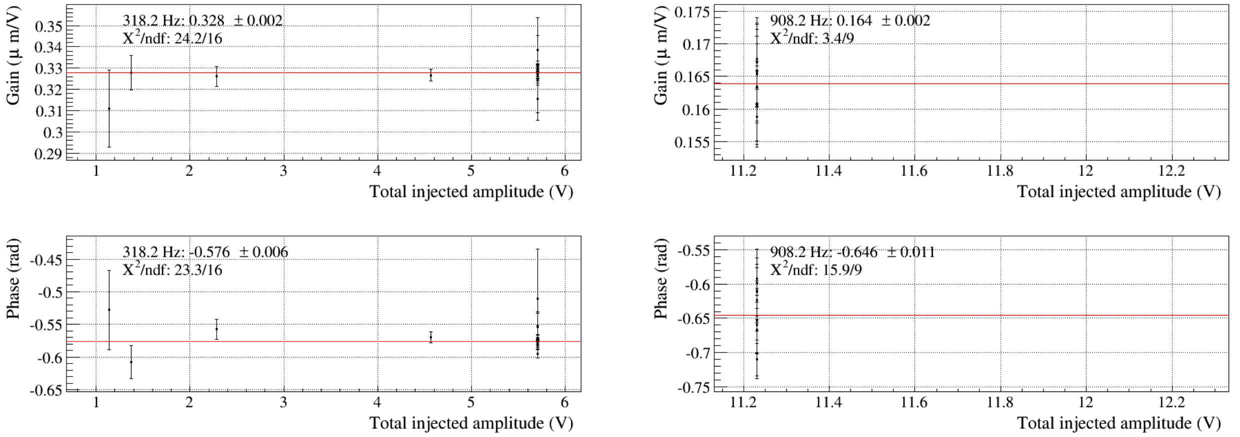

(c) ~ 317 Hz

(d) ~ 907 Hz

Figure 33: Response of the NI mirror actuation as function of the amplitude of the injected signal at four different frequencies.

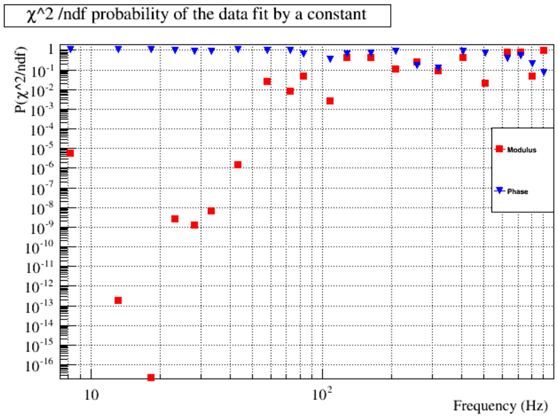

(a) χ^2 probabilities

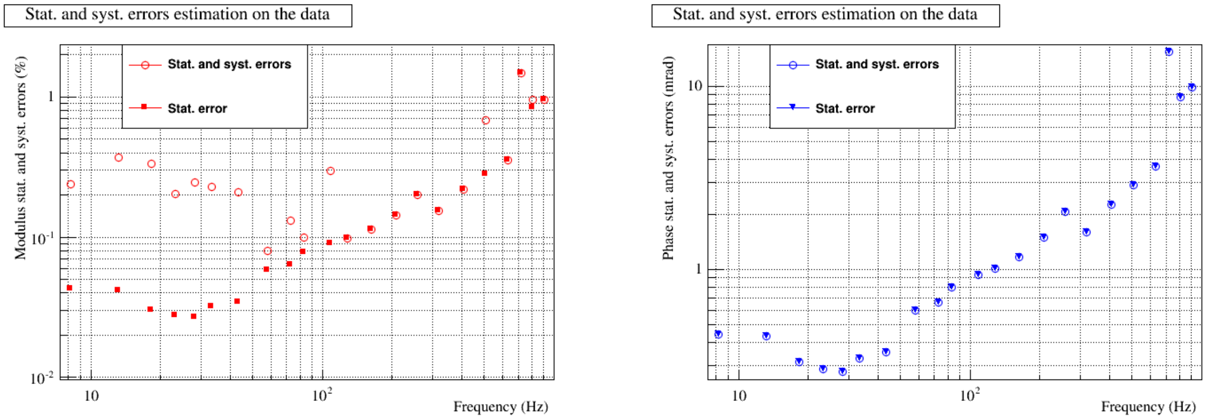

(b) Estimated uncertainties on the modulus (c) Estimated uncertainties on the phase

Figure 34: Estimation of the systematic errors coming from time variations of the measurements for the NI actuation response measured in short Michelson data. (a) χ^2 *probability of the fit of the data by a constant vs time at every frequencies. (b) stat. and sum of stat. and syst. errors to be added in order to have data compatible with a constant in time for the modulus. (c) same for the phase..*

C.3 BS mirror actuation

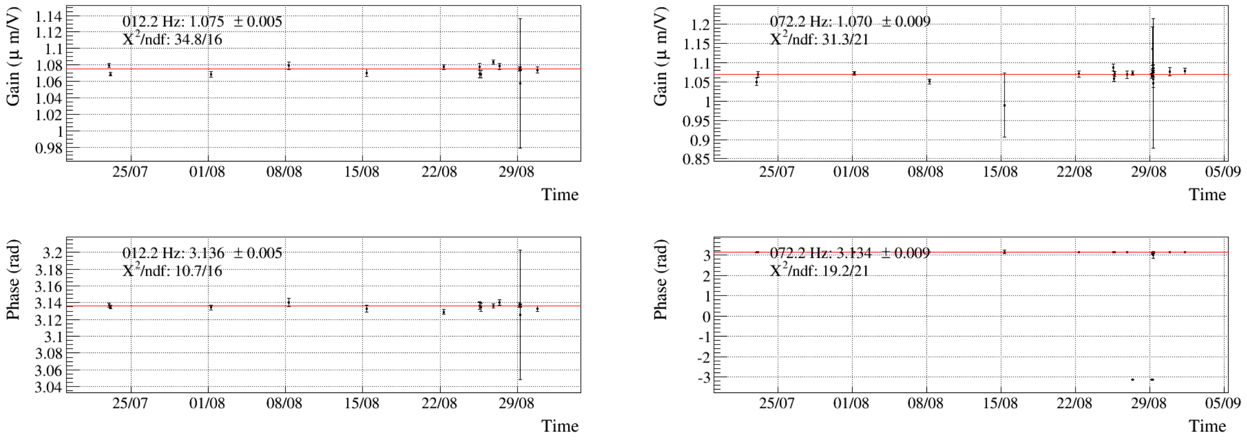

(a) ∼ 12 Hz (b) ∼ 42 Hz

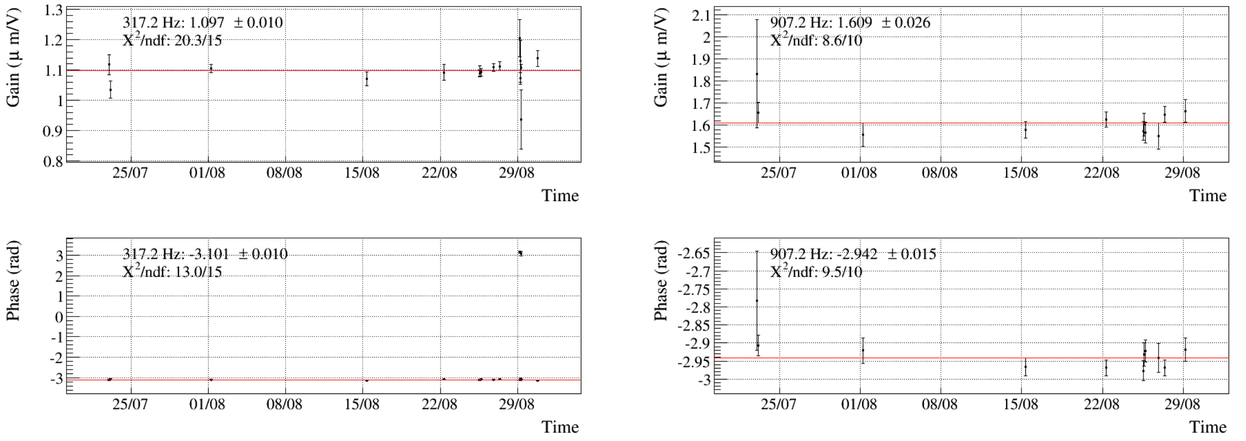

(c) ∼ 317 Hz (d) ∼ 907 Hz

Figure 35: Response of the BS mirror actuation as function of time at four different frequencies.

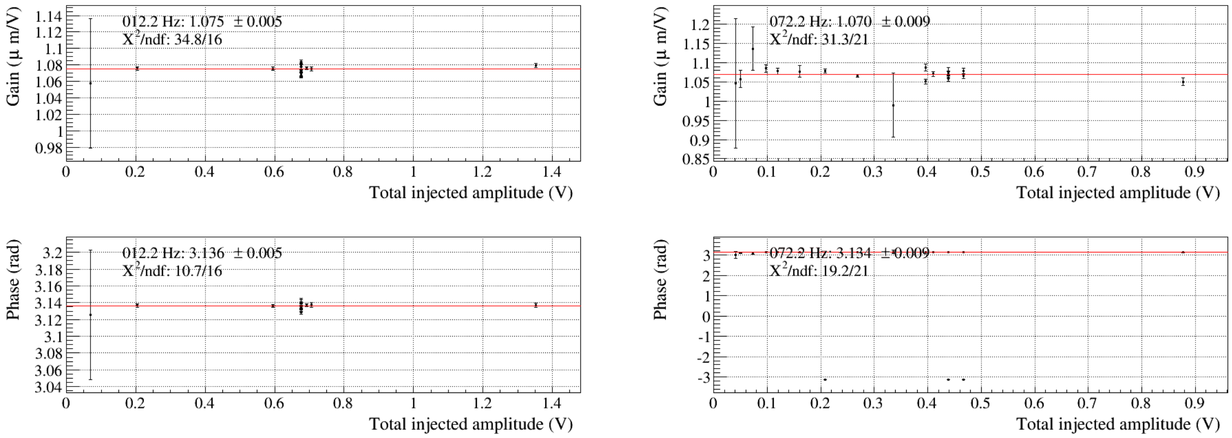

(a) ∼ 12 Hz (b) ∼ 42 Hz

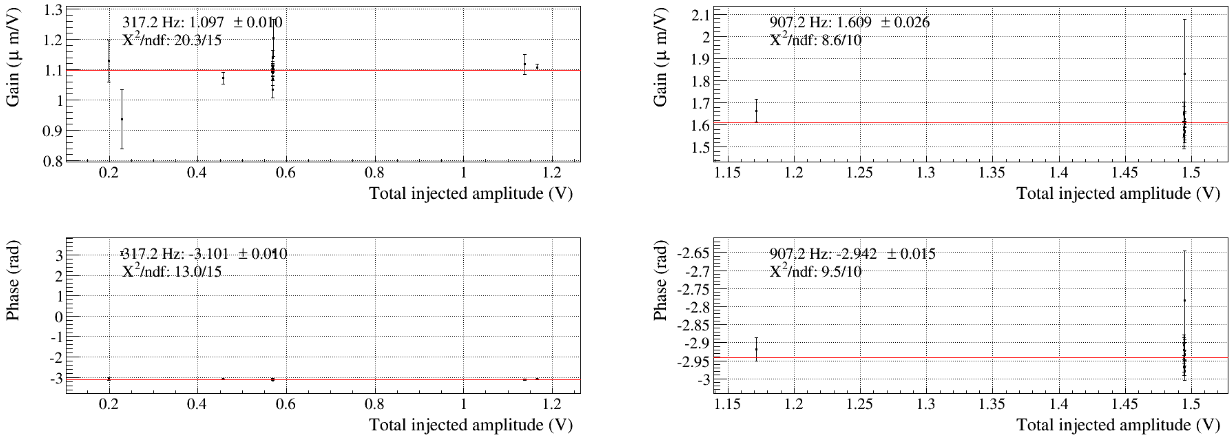

(c) ∼ 317 Hz (d) ∼ 907 Hz

Figure 36: Response of the BS mirror actuation as function of the amplitude of the injected signal at four different frequencies.

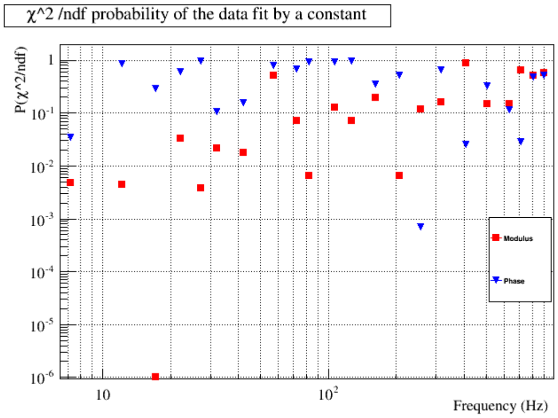

(a) χ^2 probabilities

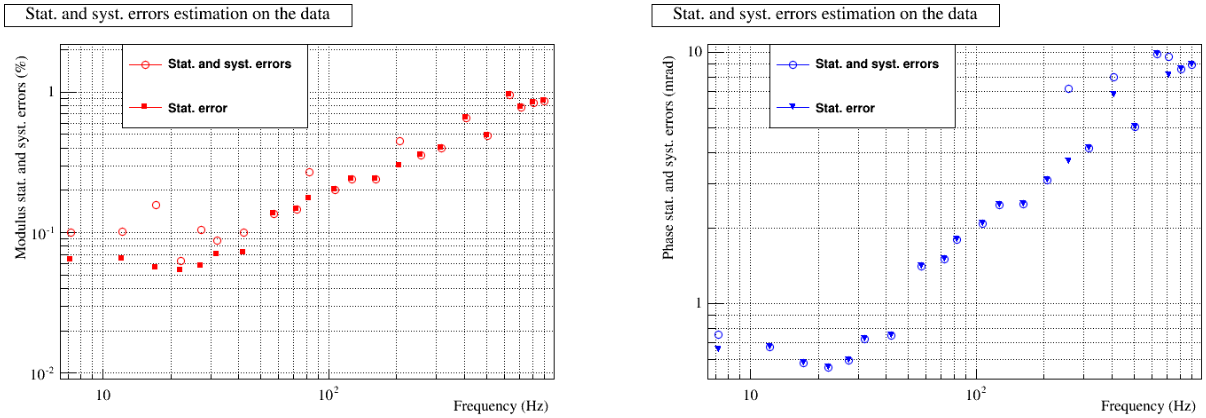

(b) Estimated uncertainties on the modulus

(c) Estimated uncertainties on the phase

Figure 37: Estimation of the systematic errors coming from time variations of the measurements for the BS actuation response measured in short Michelson data. (a) χ^2 probability of the fit of the data by a constant vs time at every frequencies. (b) stat. and sum of stat. and syst. errors to be added in order to have data compatible with a constant in time for the modulus. (c) same for the phase..

D Stability of input to end mirror calibration transfer measurements: figures

D.1 WI to WE calibration transfer

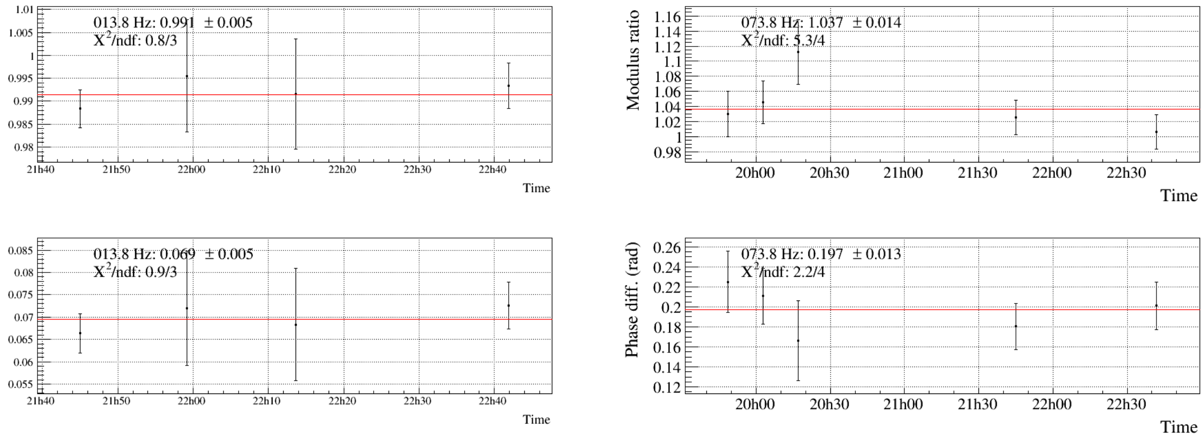

(a) ~ 12 Hz (b) ~ 42 Hz

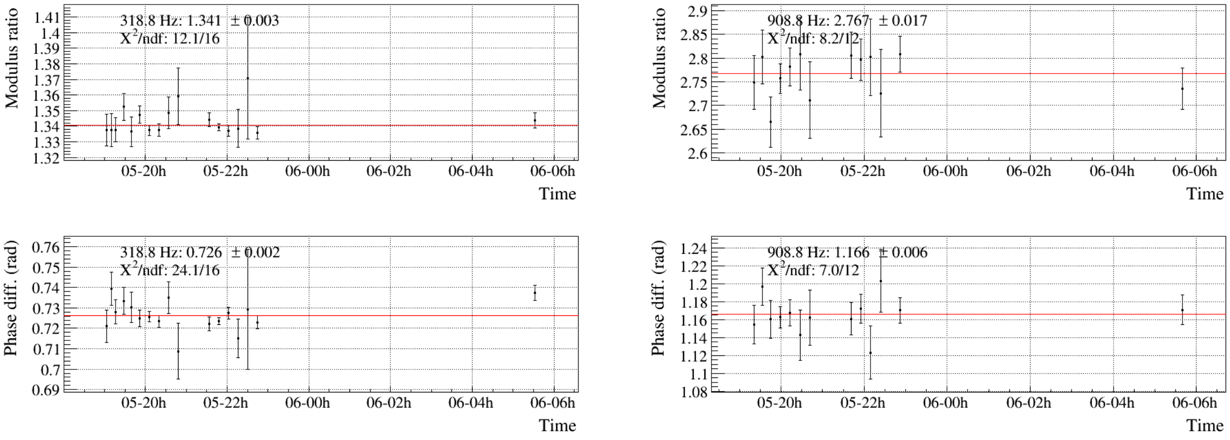

(c) ~ 317 Hz (d) ~ 907 Hz

Figure 38: Ratio of the WI and WE actuation response as function of time at four different frequencies.

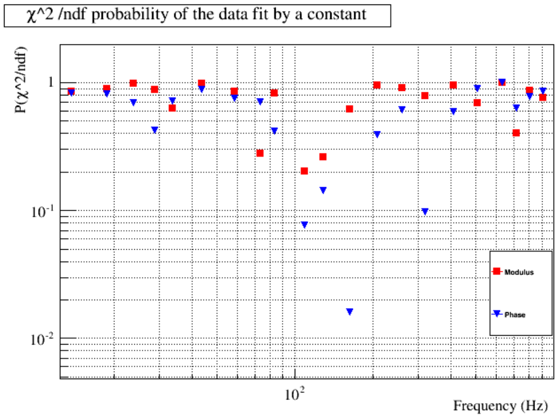

(a) χ^2 probabilities

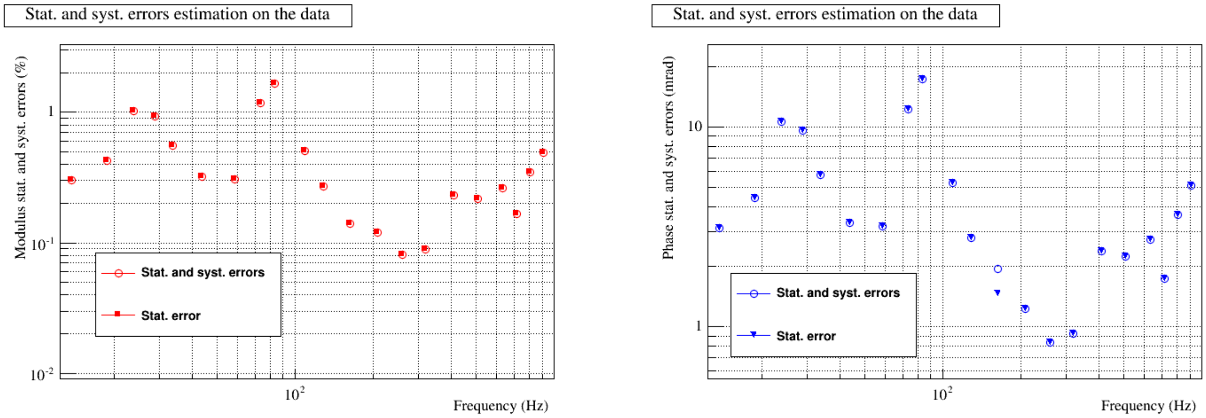

(b) Estimated uncertainties on the modulus

(c) Estimated uncertainties on the phase

Figure 39: Estimation of the systematic errors coming from time variations of the measurements for the ratio of the WI to WE actuation response. (a) χ^2 *probability of the fit of the data by a constant vs time at every frequencies. (b) stat. and sum of stat. and syst. errors to be added in order to have data compatible with a constant in time for the modulus. (c) same for the phase..*

D.2 NI to NE calibration transfer

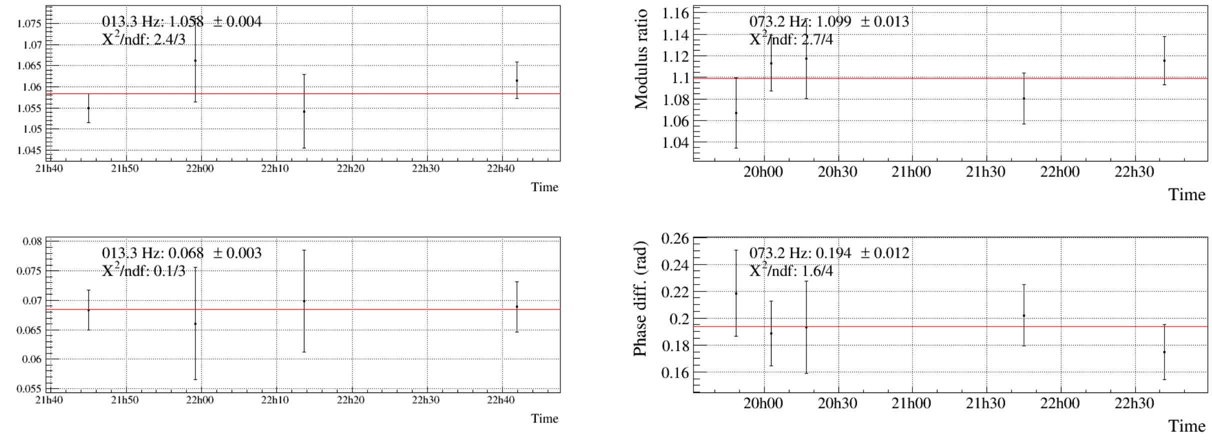

(a) ~ 12 Hz (b) ~ 42 Hz

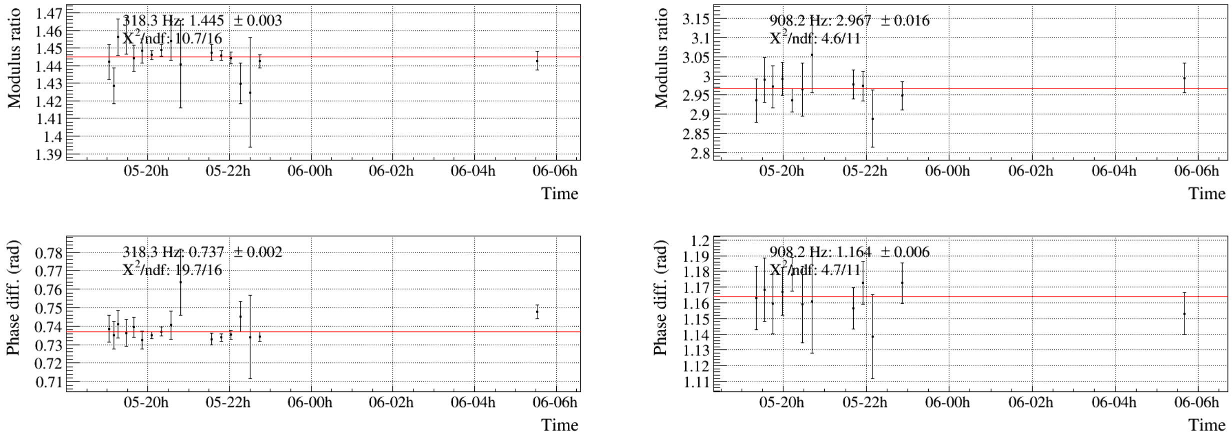

(c) ~ 317 Hz (d) ~ 907 Hz

Figure 40: Ratio of the NI and NE actuation response as function of time at four different frequencies.

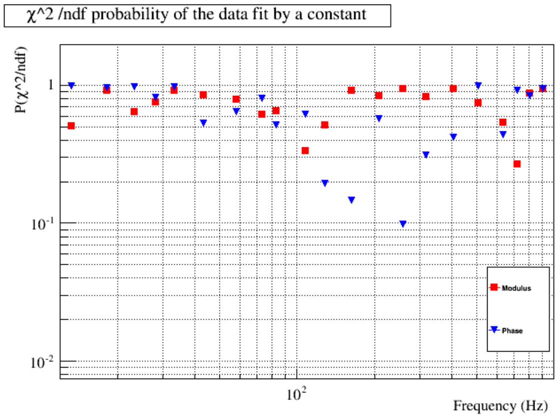

(a) χ^2 probabilities

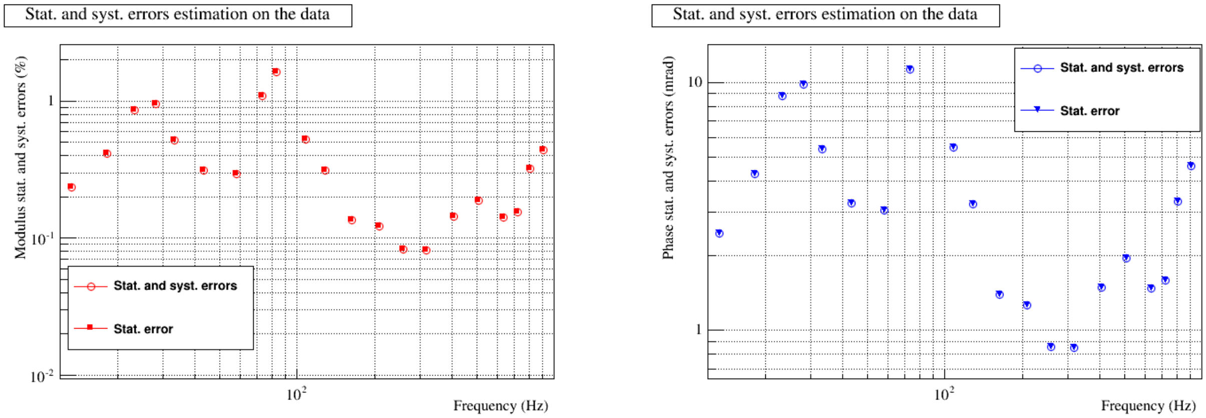

(b) Estimated uncertainties on the modulus (c) Estimated uncertainties on the phase

Figure 41: Estimation of the systematic errors coming from time variations of the measurements for the ratio of the NI to WNE actuation response. (a) χ^2 probability of the fit of the data by a constant vs time at every frequencies. (b) stat. and sum of stat. and syst. errors to be added in order to have data compatible with a constant in time for the modulus. (c) same for the phase..

E Stability of mirror to marionette calibration transfer measurements: figures

E.1 WE mirror to marionetta calibration transfer

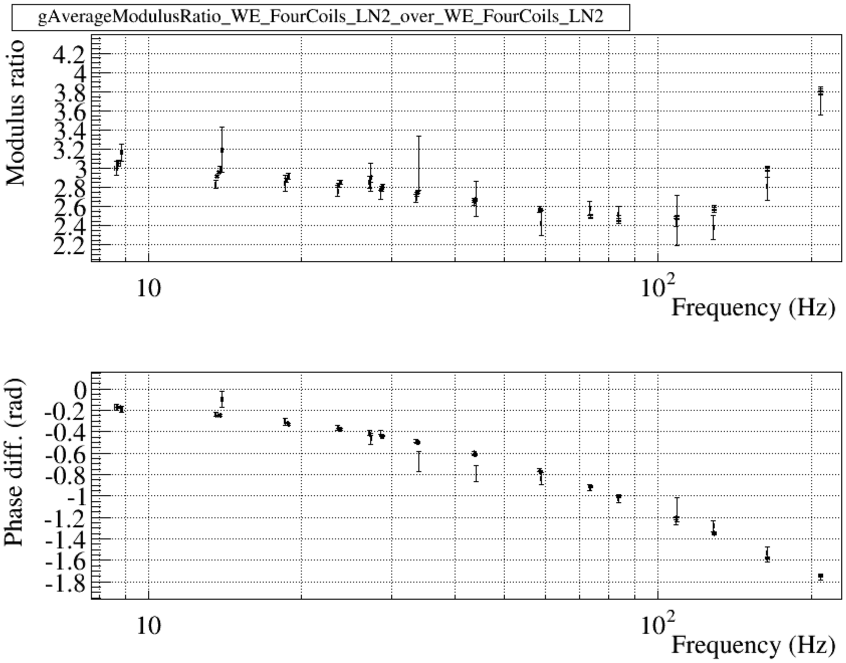

Figure 42: Averaged ratio of the WE mirror and marionette actuation responses..

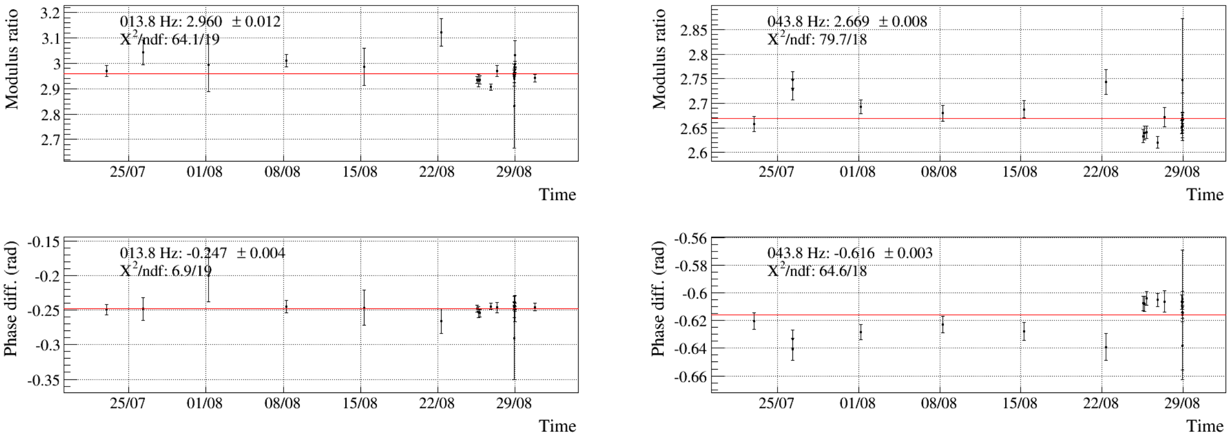

(a) ~ 12 Hz

(b) ~ 42 Hz

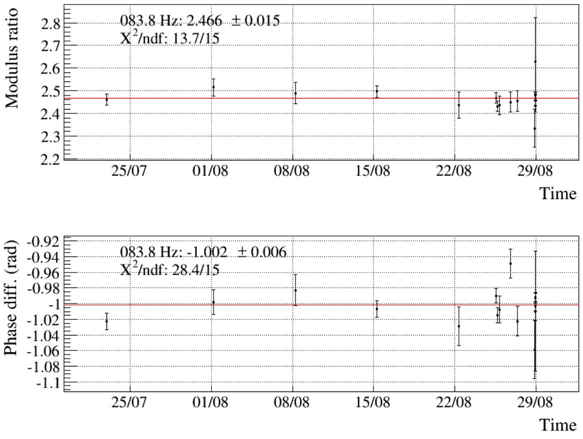

(c) ~ 82 Hz

Figure 43: Ratio of the WE mirror and marionette actuation responses as function of time at three different frequencies.

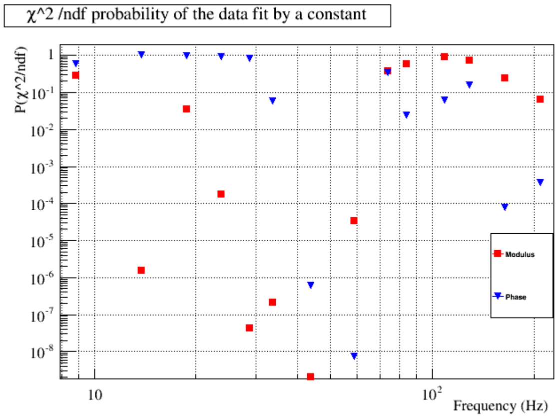

(a) χ^2 probabilities

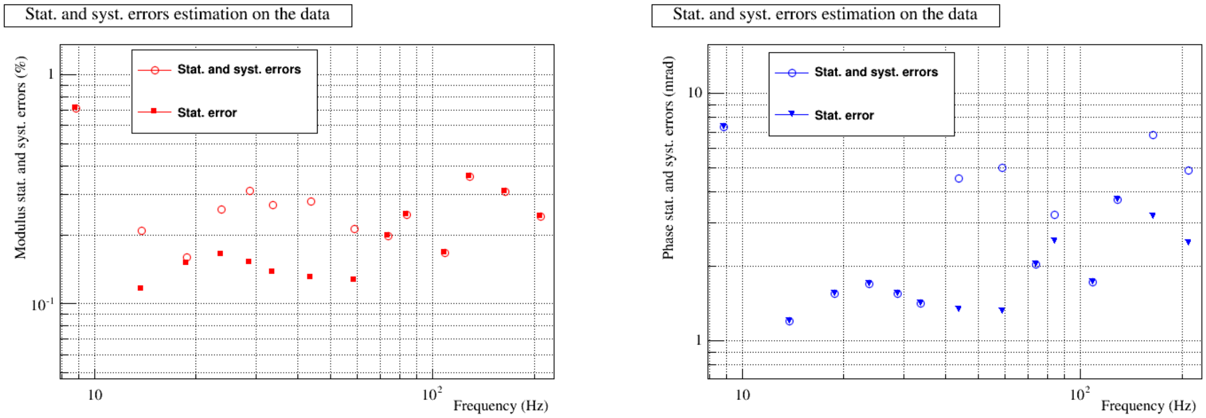

(b) Estimated uncertainties on the modulus

(c) Estimated uncertainties on the phase

Figure 44: Estimation of the systematic errors coming from time variations of the measurements for the ratio of the WE mirror to marionette actuation response. (a) χ^2 *probability of the fit of the data by a constant vs time at every frequencies. (b) stat. and sum of stat. and syst. errors to be added in order to have data compatible with a constant in time for the modulus. (c) same for the phase..*

E.2 NE mirror to marionetta calibration transfer

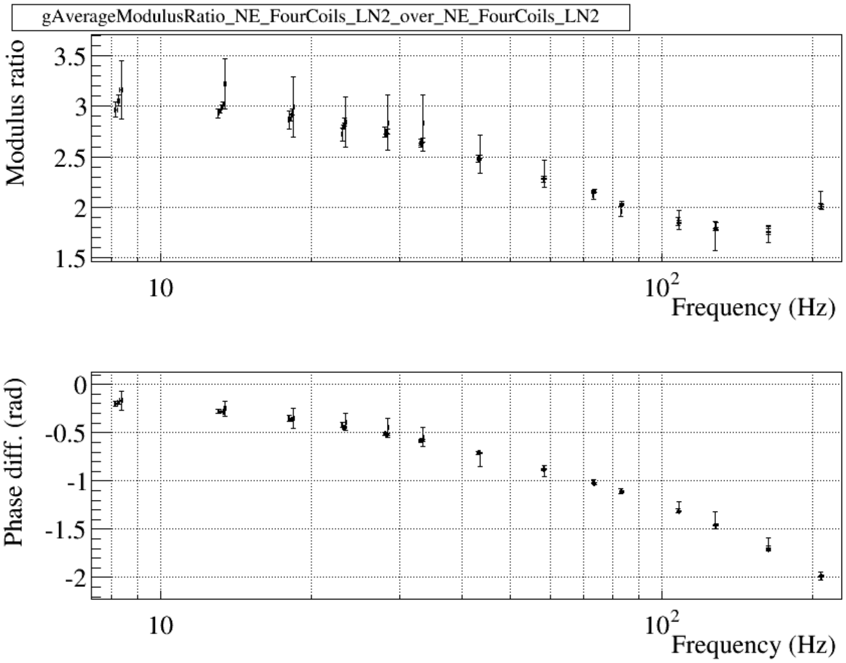

Figure 45: Averaged ratio of the NE mirror and marionette actuation responses..

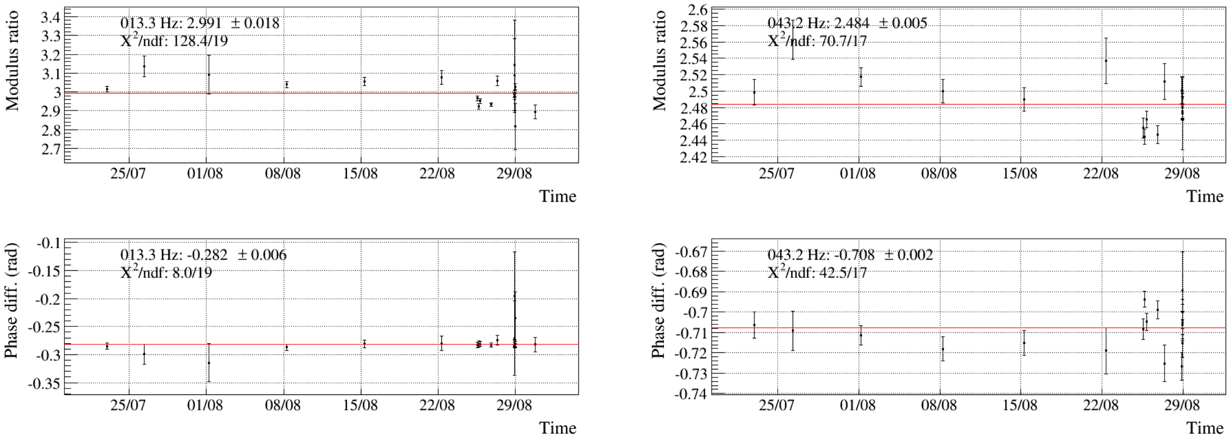

(a) ∼ 12 Hz (b) ∼ 42 Hz

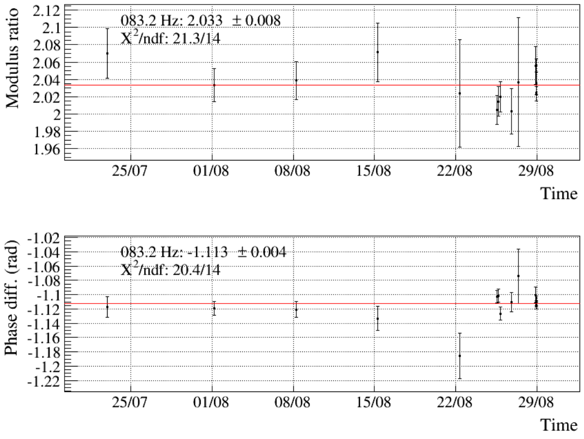

(c) ∼ 82 Hz

Figure 46: Ratio of the NE mirror and marioentte actuation responses as function of time at three different frequencies.

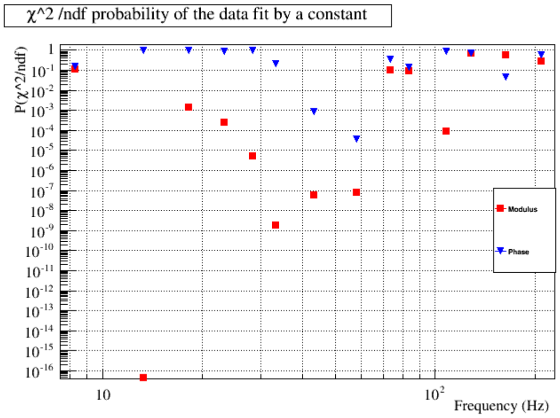

(a) χ^2 probabilities

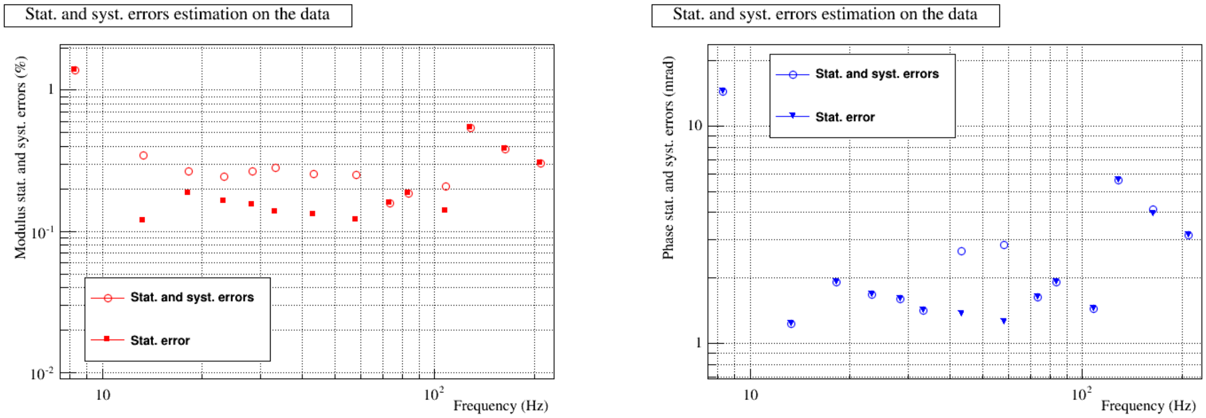

(b) Estimated uncertainties on the modulus

(c) Estimated uncertainties on the phase

Figure 47: Estimation of the systematic errors coming from time variations of the measurements for the ratio of the NE mirror to marionette actuation response. (a) χ^2 probability of the fit of the data by a constant vs time at every frequencies. (b) stat. and sum of stat. and syst. errors to be added in order to have data compatible with a constant in time for the modulus. (c) same for the phase..

E.3 BS mirror to marionetta calibration transfer

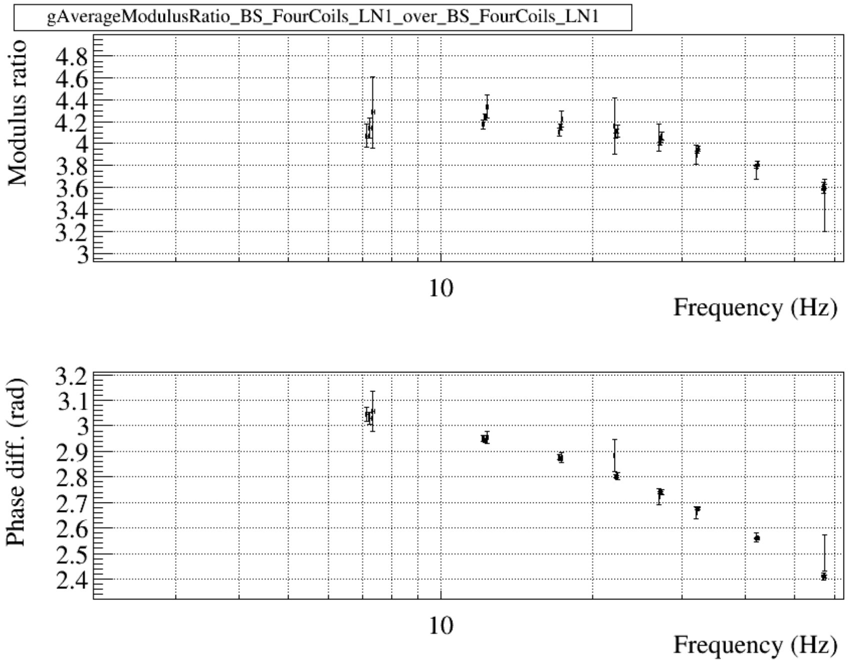

Figure 48: Averaged ratio of the BS mirror and marionette actuation responses..

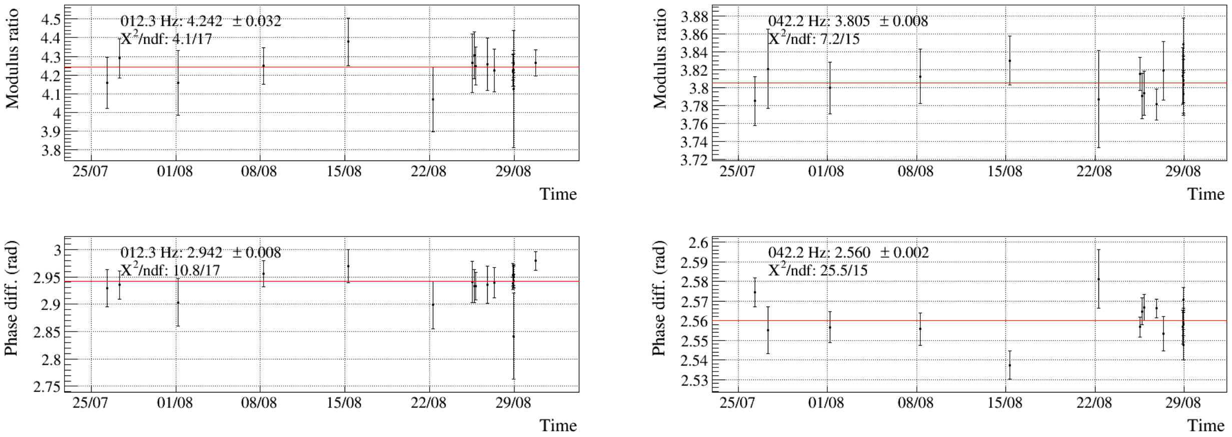

(a) ∼ 12 Hz

(b) ∼ 42 Hz

Figure 49: Ratio of the BS mirror and marioentte actuation responses as function of time at two different frequencies.

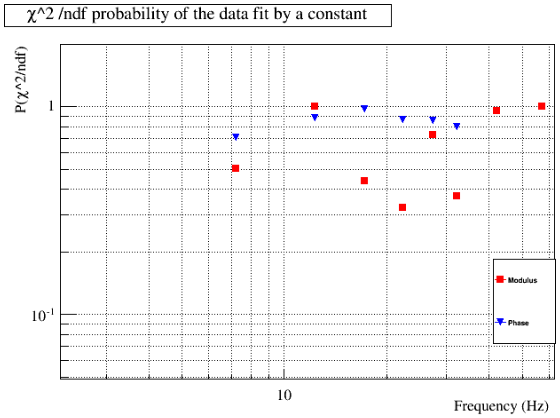

(a) χ^2 probabilities

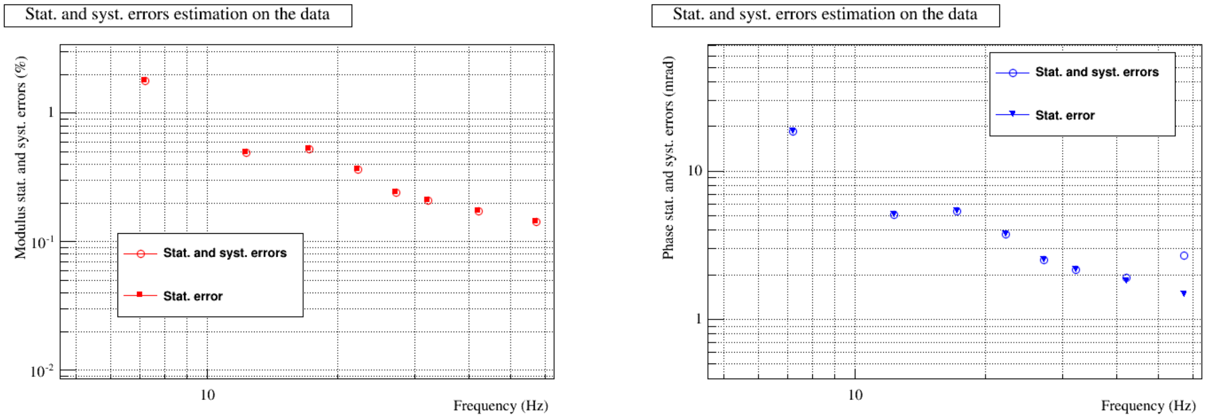

(b) Estimated uncertainties on the modulus

(c) Estimated uncertainties on the phase

Figure 50: Estimation of the systematic errors coming from time variations of the measurements for the ratio of the BS mirror to marionette actuation response. (a) χ^2 probability of the fit of the data by a constant vs time at every frequencies. (b) stat. and sum of stat. and syst. errors to be added in order to have data compatible with a constant in time for the modulus. (c) same for the phase..

F Stability of WI to PR mirror calibration transfer measurements: figures

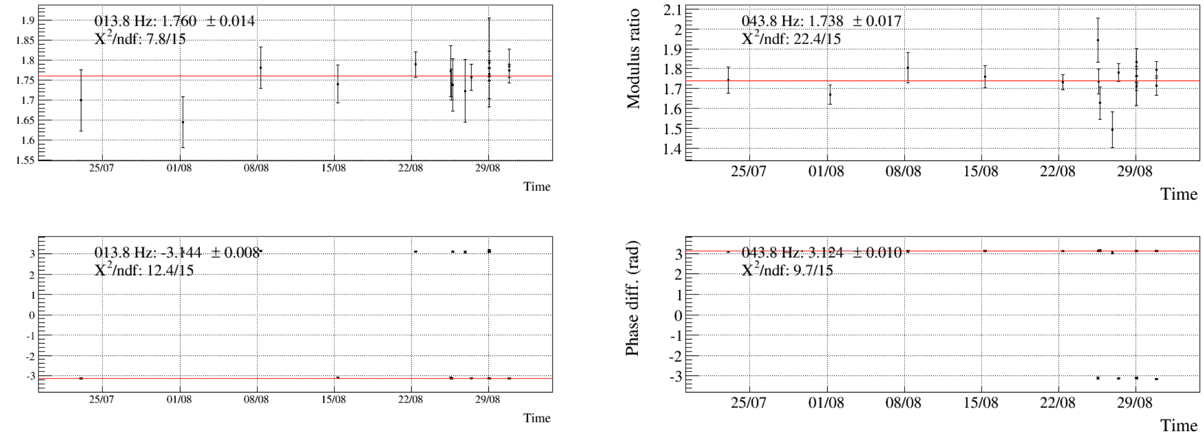

(a) ~ 12 Hz (b) ~ 42 Hz

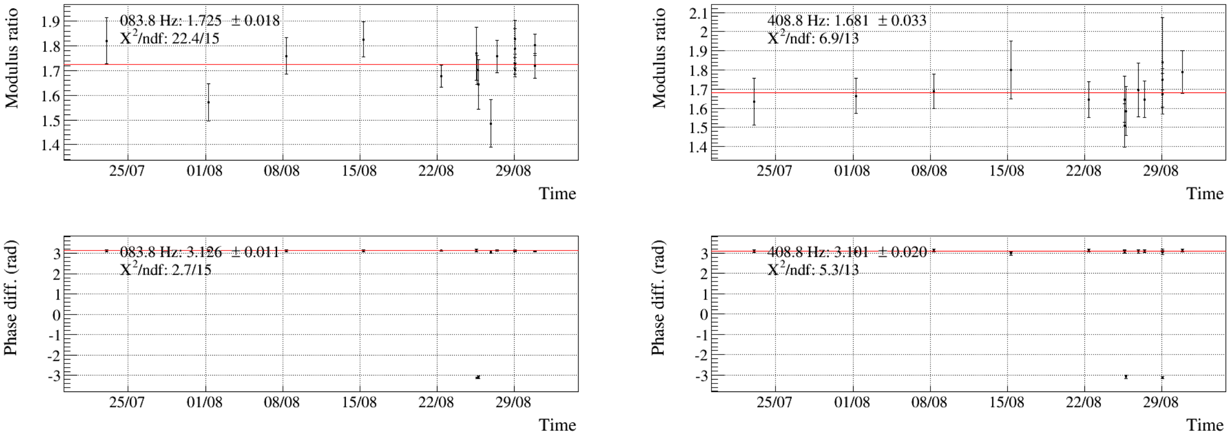

(c) ~ 82 Hz (d) ~ 907 Hz

Figure 51: Ratio of the PR and WI mirror actuation responses as function of time at four different frequencies.

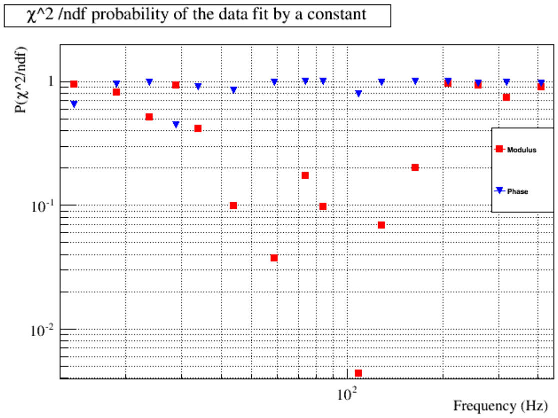

(a) χ^2 probabilities

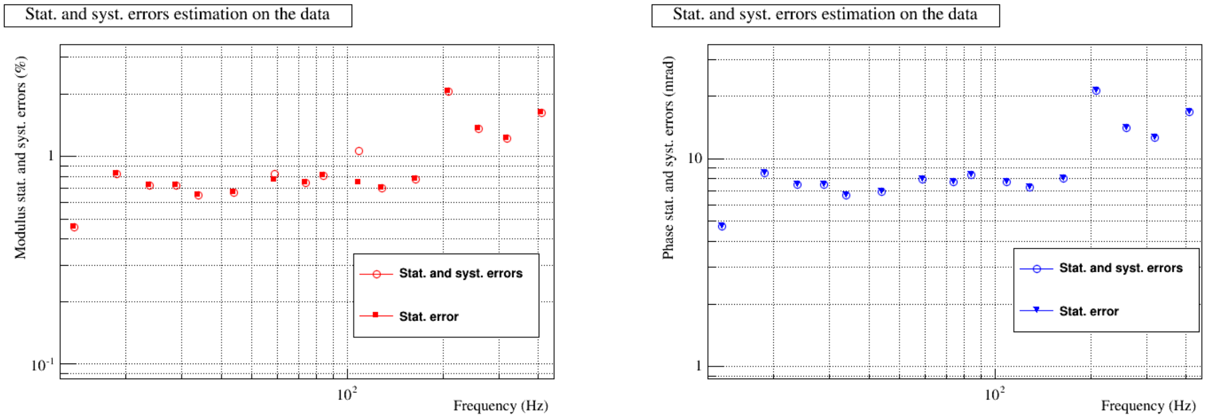

(b) Estimated uncertainties on the modulus

(c) Estimated uncertainties on the phase

Figure 52: Estimation of the systematic errors coming from time variations of the measurements for the ratio of the WI to PR mirror actuation response. (a) χ^2 probability of the fit of the data by a constant vs time at every frequencies. (b) stat. and sum of stat. and syst. errors to be added in order to have data compatible with a constant in time for the modulus. (c) same for the phase..

G Measurement of the delay from CAL to Sc actuation channels

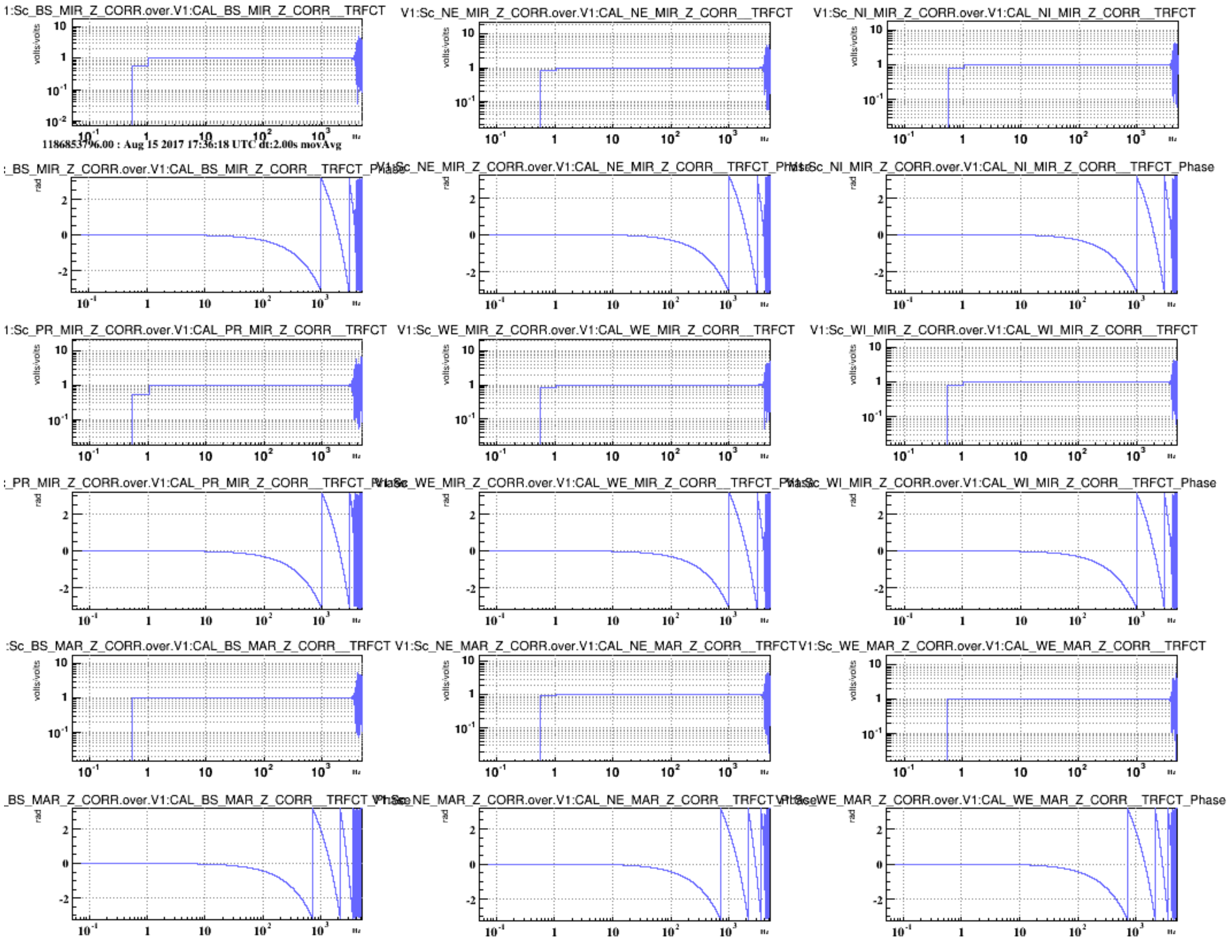

Figure 53: Measurement of the delay from the CAL to the Sc channels for the mirror and marionettes.